



Phased array guided wave propagation in curved plates



Qi Yuan ^a, Bence Kato ^a, Keqing Fan ^c, Ying Wang ^{a,b,*}

^a School of Civil and Environmental Engineering, Harbin Institute of Technology (Shenzhen), Guangdong 518055, China

^b Department of Civil and Environmental Engineering, University of Surrey, Guildford, Surrey GU2 7XH, United Kingdom

^c Wuyi University, Guangdong, China

ARTICLE INFO

Communicated by Jerome Antoni

Keywords:

Damage detection and localization
Phased array
Guided waves
Curved plate
Structural health monitoring

ABSTRACT

For the monitoring of plate structures, phased array guided wave has great application prospects to effectively determine damage location and size. Locating damage via phased array focusing is a challenging task, especially in curved plates. Hence, a systematic understanding of the behavior of the phased array guided wave propagation in curved plates is needed. In this study, a phased array focusing method was proposed for the damage localization of curved plates. Different damage scenarios and phased array focusing schemes are investigated in the finite element plate models with different radii. A high-speed signal generation and acquisition system including PZT actuators and sensors is set up. Experimental tests are carried out on a curved aluminum plate with embedded piezoelectric elements to verify the finite element models. Parametric studies are then performed to evaluate the effect of different radii and damage scenarios on the behavior of phased array guided wave propagation in curved plates. Numerical simulations and experimental results show that the proposed PA method has the capabilities of wave focusing and damage identification in curved plates. The damage localization method using phased array guided wave has the potential to be applied to the real-time monitoring of structures with curved plates.

1. Introduction

Curved plates are frequently used in aerospace engineering structures, wind turbine blades, pressure vessels, etc. The curved plates of these structures are typically operated under cycling loads and extreme temperatures. The harsh service environment may result in cracks or collapse failures [1,2], leading to significant loss of life and property. Failure of pressure vessels often occurs in the cylindrical section, i.e., curved plates. While a multitude of cracks may develop on wind turbine blades on their curved surface near the blade edge on the high-pressure side [3,4]. As curve plates are often found on multi-million-dollar equipment it is necessary to find an effective method to determine the health status of these plates.

Recently, researchers have shown an increased interest in structural health monitoring (SHM) [5,6]. Checking the safety status continuously or as needed of critical structural components and properties, the overall structural health state can be rapidly inferred [7]. SHM technology plays a paramount role in assessing structural safety while reducing all cycle management costs in various engineering fields [8,9]. Nowadays, this technology has been successfully applied to the Qingma Bridge [10], the Boeing 737 aircraft [11], and 10 MW wind turbines [12]. However, the identification and characterization of damage and deterioration in large and complex structures have proven to be an especially challenging problem for the SHM research community [13]. For example, global

* Corresponding author at: School of Civil and Environmental Engineering, Harbin Institute of Technology (Shenzhen), Guangdong 518055, China.

E-mail address: yingwang@hit.edu.cn (Y. Wang).

approaches using accelerometers and extensometers have proven to be relatively insensitive to small levels of damage [14]. Similar problems with passive SHM methods have been identified. For example, the acoustic emission approach can easily be influenced by noises that make it insensitive to damage [15,16]. While strain-based approaches are only sensitive to local area strain field changes [17]. To overcome these limitations, researchers are working on an ultrasonic guided waves approach which is an active method for detecting damage by emitting waves into the structure [18–20]. For health monitoring of plate structures, this active method has great application prospects to effectively determine the damage location and size [21].

Guided waves are elastic waves formed by wave reflection, refraction, and mode conversions at the boundaries of an object. Guided waves in plate structures can be divided into Lamb waves and SH waves according to different modes of particle displacements in the excited material. Lamb waves have been explored for damage detection in metallic plates [22], composite plates [23], and pipelines [24,25]. Lamb waves can travel long distances with little attenuation allowing them to effectively scan a large area using a transducer. Lamb wave propagation properties in plates have been widely studied using theoretical, numerical, and experimental methods [23,26]. In curved plates, guided waves can travel in the circumferential or axial direction. Guided waves propagating in the axial direction involve longitudinal waves, torsional waves, and flexural waves; in the circumferential direction, they involve circumferential Lamb type (CLT) waves and circumferential SH type (CSH) waves [27]. When the curved plate behaves more like a plate, the CLT and CSH waves will converge to Lamb and SH waves, respectively. To locate damage in a curved plate via guided waves various approaches have been proposed, including waveform analysis [28,29], and time-of-flight (ToF) [1]. ToF is defined as the wave travelling time along with the actuator–damage–sensor path [30].

In general, the multiple modes of CLT waves and their dispersion nature can make damage identification complicated, which means it is difficult to interpret in a measured waveform. Moreover, it is hard to distinguish a waveform generated by damage from that by boundary reflection [31]. To overcome these challenges, phased array (PA) techniques can be used to focus the guided waves generated by piezoelectric elements to enhance damage localization and characterization [32]. Unlike methods that employ a single piezoelectric element, PA techniques rely on multiple piezoelectric elements assembled in linear or grid arrays and can focus the guided waves at a predefined focal point in the structure. Specifically, varying the waveform phase via artificially adding time delay to the excitation signal and operating each piezoelectric element at the same time can result in constructive interference of the emitted waves, which creates a wavefield with the desired direction [33]. Both linear and grid PA setups have been reported in the literature on SHM [26,34,35] for detecting damage in plates but few researchers have studied this method in curved plates [31,36]. Moreover, the systematic understanding of the behavior of PA guided wave propagation in curved plates is still missing for SHM purposes.

Since aluminum is one of the most commonly used materials for plate structures, therefore, aluminum curved plates were studied in this paper. The finite element method (viz. ABAQUS) was used to simulate the PA guided wave propagation in the curved plates. To verify the numerical simulations, a highly precise time synchronization acquisition system was developed for experimental purposes. The experimental tests were carried out on a curved plate with embedded piezoelectric elements. The piezoelectric elements are used to generate high-frequency pulse forces on the curved plate and to record the PA guided wave propagation signals. Test results are compared with the numerical simulation results to check the performance of the finite element models. The radius of the model curved plates, damage location and size were varied. The various models were utilized to assess the focusing ability and damage detection accuracy of the PA method. Parametric simulations are also performed to evaluate the effect of different plate radii and damage scenarios on the propagation of the PA guided wave. Numerical simulations and experimental results show that the PA method has the capabilities of wave focusing and damage identification in curved plates with different radii.

2. Theoretical background

2.1. Dispersion characteristics of CLT waves in curved plates

A curved plate can be regarded as a portion of a hollow cylinder. CLT waves are suited for damage detection as they are sensitive to material defects in hollow cylinders [27]. Thus, as a kind of guided wave, they can be employed for long-distant inspections. These properties are attractive for SHM because a limited number of PZT transmitters can be utilized to detect damages within a large area of complex, curved surfaced structures. Due to the radius of curved plates, it is difficult to distinguish symmetric and anti-symmetric modes. Therefore, we use the subscript m in CLT_m to designate the wave mode number.

Circumferential guided waves are guided waves that propagate in the circumferential direction of the hollow cylinder. A practical application of them in SHM is the detection of corrosion in piping from in-pipe or in-line inspection vehicles.

The circumferential guided wave dispersion equation of hollow cylindrical structures with traction-free surfaces is written as [27,37]:

$$|D(k, \omega)| = 0 \quad (1)$$

$D(k, \omega)$ is a 4×4 matrix, which is the function of frequency, ω , and wavenumber, k , the individual components of it are provided in Appendix A. $J_k(x)$, $Y_k(x)$ are k^{th} order first and second Bessel functions while, η , κ , \hat{k} and $\hat{\omega}$ are defined as.

$$\eta = \frac{a}{b} \quad (2)$$

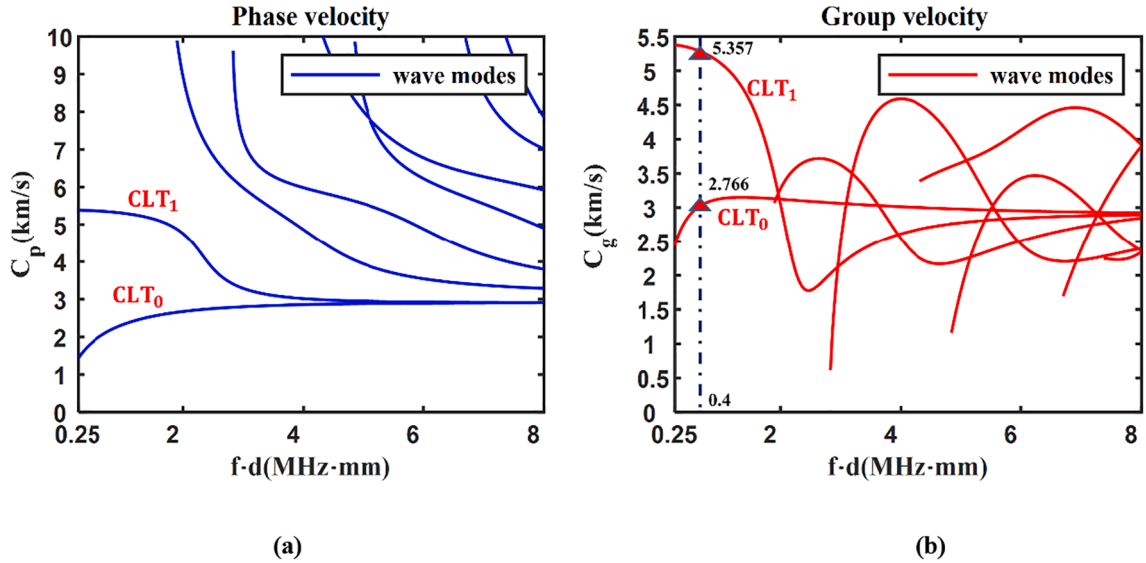


Fig. 1. Equivalent Dispersion curves of CLT waves in an aluminum plate with a radius of 250 mm: (a) phase velocity, c_p , and (b) group velocity, c_g , of multiple wave modes.

$$\kappa = \frac{c_L}{c_T} = \sqrt{\frac{2(1-\nu)}{(1-2\nu)}} \quad (3)$$

$$\hat{k} = kb \quad (4)$$

$$\hat{\omega} = \frac{\omega b}{c_T} \quad (5)$$

where ν is the Poisson ratio, a and b are the inner and outer diameters of the curved plate, respectively. c_L is the longitudinal wave velocity, c_T is the shear wave velocity in the plate material. The phase (c_p) and the group (c_g) velocities of CLT waves vary with the frequency-wall thickness $f \cdot d$.

For a given angular frequency, the characteristic equations can be solved numerically to find the real wavenumber and the CLT wave mode phase velocity, $c_p = \omega/k$. The group velocity is defined as $c_g = d\omega/dk$ and can be written in terms of c_p .

$$c_g = c_p^2 \left(c_p - f \cdot d \frac{dc_p}{d(f \cdot d)} \right)^{-1} \quad (6)$$

CLT waves and Lamb waves are essentially two different guided waves. The differences between them are obvious when the ratio of the inner and outer diameters of a curved plate decrease. Therefore, the corresponding dispersion curves must be solved according to the specific inner and outer diameters. For a curved plate with a ratio of radius to wall thickness is no more than about 20, the dispersion curves can be quickly determined using DISPERSE. If this ratio is greater than about 20, DISPERSE will diverge while attempting to find the roots for the Bessel functions. When this occurs, the curved plate can alternatively be modelled as a flat plate and the solutions remain the same. This is because when the arguments of the Bessel functions are large enough to cause instability, they can be considered as damped versions of their Cartesian counterparts and provide very similar results. A general rule of thumb, according to our test results, is that a plate can be considered flat when the minimum frequency of interest is greater than the value given by Eq. (7) [38].

$$f_{min} = \frac{v_{long}}{r_{inner}} \quad (7)$$

where f_{min} is the minimum frequency in MHz, r_{inner} is the inner radius of the curved plate in mm, and v_{long} is the plate material's bulk longitudinal velocity in mm/ μ s. Therefore, if the target application will only use frequency-wall thicknesses above 0.25 mm-MHz, a plate can be replaced when the ratio of radius to wall thickness is greater than about 20. Since an excitation frequency of 100 kHz and a plate thickness of 4 mm are used in this study, the resulting dispersion curves only are considered above the frequency-wall thickness of 0.25 MHz • mm. At the same time, the minimum ratio of radius to wall-thickness of the studied curved plates is 62.5. Therefore, the two conditions mentioned above are satisfied. The dispersion curves of the curved plates studied herein are the same as that of a flat plate whose frequency-wall thickness is also greater than 0.25 MHz • mm, codes that can calculate dispersion curves already have the dispersion curve information which is presented in Fig. 1.

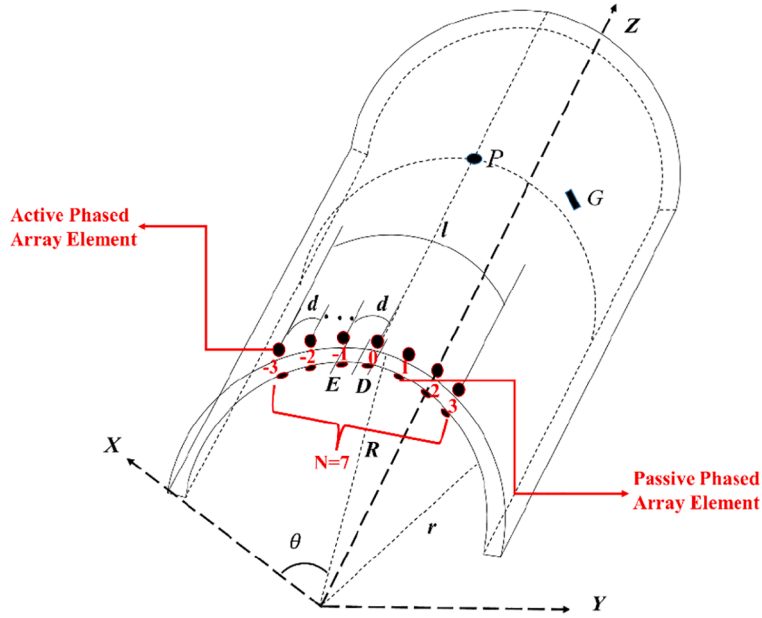


Fig. 2. Diagram of curved plate model and PZT element layout in the cylindrical coordinate system.

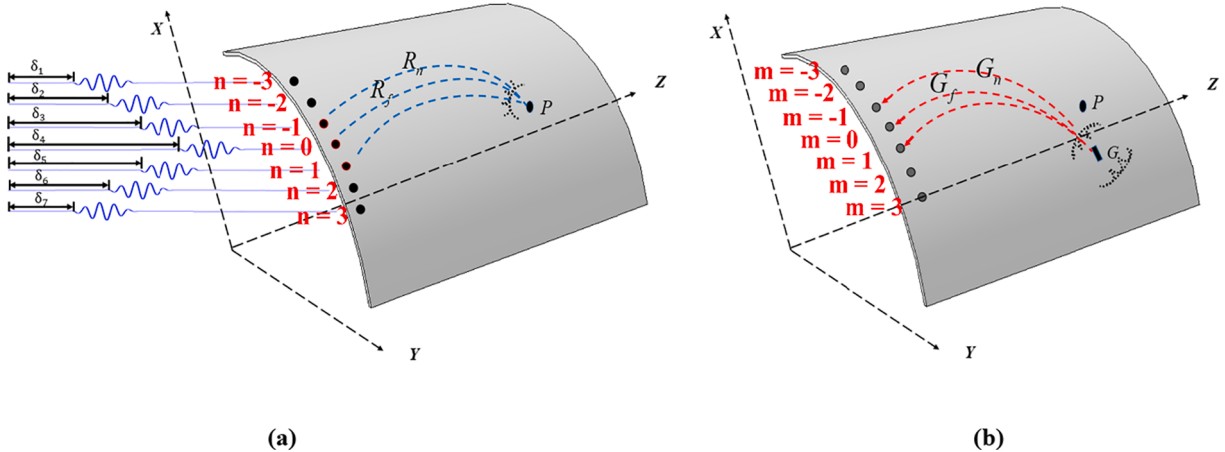


Fig. 3. Schematic diagram of curved plate PA focusing and damage localization theory: (a) directional propagate to a focal point P; (b) back-scattered wave from damage at G.

2.2. PA focusing theory of curved plate

The PA guided wave in solid media was inspired by the concept of scanning antenna arrays used in radar systems. Nowadays, PA techniques are widely used in the civil engineering industry to identify material defects and structural damage in a non-destructive manner [39].

For active PA, each element can be parallelly excited with the desired waveform. The PA applies predefined waveforms to ensure that the waves generated by each element constructively interfere in the physical domain. The generated interference pattern leads to directional guided waves focused on a specific area of the structure. PA guided wave focused on the damaged region will reflect and scatter. These reflected waves are then detected by the passive PA (i.e., the receiver). The received waveform is post-processed and judgment is made on whether there is any damage in that area. The active PA elements are excited individually with a phase shift between their actuation, to develop a controllable waveform focused on the desired location.

The multi-wave mode feature of guided waves makes the propagation of PA guided waves very complex in curved plates. To simplify mode analysis, a 100 kHz five-cycle sinusoidal tone-burst signal enclosed in the Hanning window is chosen as the basic excitation signal. As we can see in Fig. 1, 100 kHz corresponds to merely-two modes, the CLT₀ mode, and the CLT₁ mode, which can make subsequent signal analysis simple.

During health monitoring, the PA has an ordered arc-linear array of piezoelectric elements bonded to the inspected structure. The schematics of a curved plate are shown in Fig. 2. N is the number of PZT elements and n is the index number of each PZT element. The arc length of the curved plate is labelled as L . R is the outer diameter of the curved plate, while r is its inner diameter. d is the central arc distance between the elements. Considering the diameter, D , of the PZT elements and the arc distance, E , between the PZT elements, then $d = D + E$. Finally, the arc length of the entire PA is $l = (N-1) \cdot d$. In this study, a true active PA system with N pieces of PZT elements that are bonded to the upper surface of the curved plate is utilized. Each PZT element can be addressed for actuation. Furthermore, a true passive PA system of N pieces of PZT elements bonded to the lower surface of the curved plate is also utilized. Each of these lower PZT elements can be addressed for sensing. The index n depends on the distance between the PZT element and the centerline of the PA. For instance, if there are an odd number of PZT elements, the element in the center of the PA is indexed 0, and the PZT elements on its left are indexed $-1, -2, -3$, while the elements on its right are indexed $1, 2, 3$, in turn. If the total element number is even, then the two center elements are numbered -1 and 1 , while the elements on the left side of them are numbered $-2, -3$, and the elements on the right side of them are numbered $2, 3$, in turn.

According to the cylindrical coordinate system, we can define the coordinate of the focal point, (R, θ, z) , and the n^{th} PZT's coordinate as $(R, \frac{0.5L+nd}{R}, 0)$. To determine the time delay associated with each PZT element, δ_n , two parameters must be considered, the group velocity of the chosen mode and the distance from the element to the focal point of the PA, R_n . The distance from the n^{th} PZT element in the PA to the focal point is R_n , as Fig. 3 (a) shows. The distance is equal to:

$$R_n = \sqrt{z^2 + \left[\left(\theta - \frac{0.5L+nd}{R} \right) R \right]^2} \quad (n = 0, \pm 1, \pm 2, \dots \pm \frac{N-1}{2}) \quad (8)$$

Similarly, the distance from the focal point to the central element of the PA is:

$$R_f = \sqrt{z^2 + \left[\left(\theta - \frac{0.5L}{R} \right) R \right]^2} \quad (9)$$

When the focal point is fixed at P , the time delay δ_n corresponding to each array element can be defined. To ensure a positive time delay, a sufficiently constant t_0 must be chosen. The purpose of introducing the max function is to find the maximum value of R_n , and to make t_0 a positive number. Therefore, δ_n can be expressed as the following formula:

$$t_0 = \frac{\text{Max}(R_n) - R_f}{C_g} \quad (10)$$

$$\delta_n = t_0 + \frac{R_f}{C_g} - \frac{R_n}{C_g} \quad (11)$$

The amplitude of the waveform will attenuate as a function of $\sqrt{R_n}$. Therefore, the summation of wave amplitudes at the focal point is:

$$S_p(t) = \sum_{n=-(N-1)/2}^{n=(N-1)/2} \frac{A_n}{\sqrt{R_n}} \cdot S_0 \left(t - \frac{R_n}{C_g} - \delta_n \right) \left(n = 0, \pm 1, \pm 2, \dots \pm \frac{N-1}{2} \right) \quad (12)$$

where S_0 corresponds to the base waveform which is then shifted in time to account for the waveform travel time, and A_n is a scalar factor adjusting the amplitude of the waveform generated by the n^{th} PA element.

2.3. PA damage localization theory of curved plate

Assuming that damage exists in the curved plate at site G , with the distance G_n to the center of the passive PA, as shown in Fig. 3 (b). If damage is located at (R, θ_d, Z_d) , the wavefield will form a strong back-scattered echo with a high SNR, as previously discussed. The wave amplitude launched by the active PA focusing on the damaged site is represented by the formulation:

$$S_G(t) = \sum_{n=-(N-1)/2}^{(N-1)/2} \frac{A_n}{\sqrt{G_n}} - S_0 \left(t - \frac{G_n}{C_g} - \delta_n \right) \left(n = 0, \pm 1, 2, \dots \pm \frac{N-1}{2} \right) \quad (13)$$

where the distance from the n^{th} PZT to the damage site, G_n , is:

$$G_n = \sqrt{z_d^2 + \left[\left(\theta_d - \frac{0.5L+nd}{R} \right) R \right]^2} \quad (n = 0, \pm 1, \pm 2, \dots \pm \frac{N-1}{2}) \quad (14)$$

When there is damage at G , the reflected wave will be received by the passive PA. Let the scattering coefficient be B , and consider the attenuation term of the propagated wave amplitude as $\frac{1}{\sqrt{G_m}}$, the signal received by the m^{th} element of the passive PA can be described by [40]:

Table 1

Parameters of the aluminum curved plate.

Item	Density [kg/m ³]	Modulus [MPa]	Poisson's Ratio	Radius [mm]	Width [mm]	Length [mm]	Thickness [mm]
Value	2700	69,000	0.33	125	400	400	4

$$S_m(t) = \sum_{-(N-1)/2}^{(N-1)/2} \frac{B}{\sqrt{G_m}} - \frac{A_n}{\sqrt{G_n}} - S_0 \left(t - \frac{G_n + G_m}{c_g} - \delta_n \right) \left(n, m = 0, \pm 1, 2, \dots, \frac{N-1}{2} \right) \quad (15)$$

where the distance from the damage site G to the nth PZT is:

$$G_m = \sqrt{z_d^2 + \left[\left(\theta_d - \frac{0.5L + md}{R} \right) R \right]^2} \left(m = 0, \pm 1, \pm 2, \dots, \pm \frac{N-1}{2} \right) \quad (16)$$

The focal length G_f is the distance from the damage site G to the center of the PA:

$$G_f = \sqrt{z_d^2 + \left[\left(\theta_d - \frac{0.5L}{R} \right) R \right]^2} \quad (17)$$

The reflected waves will have different time delays at each element. To calculate the specific damage position, it is necessary to assemble and superimpose the signals received by each PZT element in the passive PA according to their different focal distances to get the location of the damage. To superimpose the received signals, the signal received by the center PZT element is taken as the reference. Then the received signals of the other elements are adjusted to match the phase of the reference signal (as they each were generated with a time delay), and then all corrected signals are simply superimposed to emphasize the amplitude of the signal indicating the damage in the structure. If the structure is an ideal curved plate with infinite boundaries and no damage, the passive PA will not receive a back-scattered wave. Furthermore, if there is damage at the focal point, the energy of the superimposed signal will have a significant magnitude that is very easy to detect. According to this theory, the superimposed signal is described as:

$$S_R(t) = \sum_{-(N-1)/2}^{(N-1)/2} S_m(t + \delta_m) \left(m = 0, \pm 1, \pm 2, \dots, \pm \frac{N-1}{2} \right) \quad (18)$$

δ_m can be written as:

$$\delta_m = \frac{G_f}{c_g} - \frac{G_m}{c_g} \quad (19)$$

3. Numerical simulation

3.1. Simulation method

To evaluate the proposed PA method for damage detection, numerical simulations of the curved plates with a radius of 125 mm were carried out. The parameters of the models are listed in Table 1. In the numerical simulation, since we focus on verifying the proposed PA method, it is not necessary to use 7 elements in the active or passive PA. The active PA elements are not explicitly modelled, instead, they are represented by loading nodes on one edge of the plate [31,41]. The passive PA is modelled by displacement (recording) nodes at the corresponding position directly below each loading node. The arc distance between each node is set at 23.4 mm.

The finite element models were built in ABAQUS. An elastic explicit dynamic analysis was carried out to simulate the guided wave propagation. A structured mesh is adopted for spatial discretization of the curved plate, consisting of linear 8-noded solid hex elements [42]. To achieve the necessary frequency resolution, the mesh size should conform to the following equation [43]:

$$\Delta x \leq \frac{1}{10} \lambda_{\min} = \frac{c_p}{10f_{\max}} \quad (20)$$

where Δx is the maximum distance between two interpolation points, λ_{\min} is the minimum wavelength of the guided wave, and f_{\max} is the excitation frequency of the ultrasonic guided wave. According to the group velocity in the dispersion curves, the minimum wave velocity of the guided wave is 2766 m/s at 100 kHz, thus the maximal edge length of the elements is:

$$\Delta x \leq \frac{c_{\min}}{10f_{\max}} = \frac{2766}{10 \times 100000} = 2.766 \text{ mm} \quad (21)$$

Note that the edge length of the elements should be as large as possible to ensure the efficiency of the simulations. Thus, the mesh grid size is set to 2.5 mm in all models.

The time increment has to be determined to ensure the numerical stability of the explicit time integration scheme. The time step

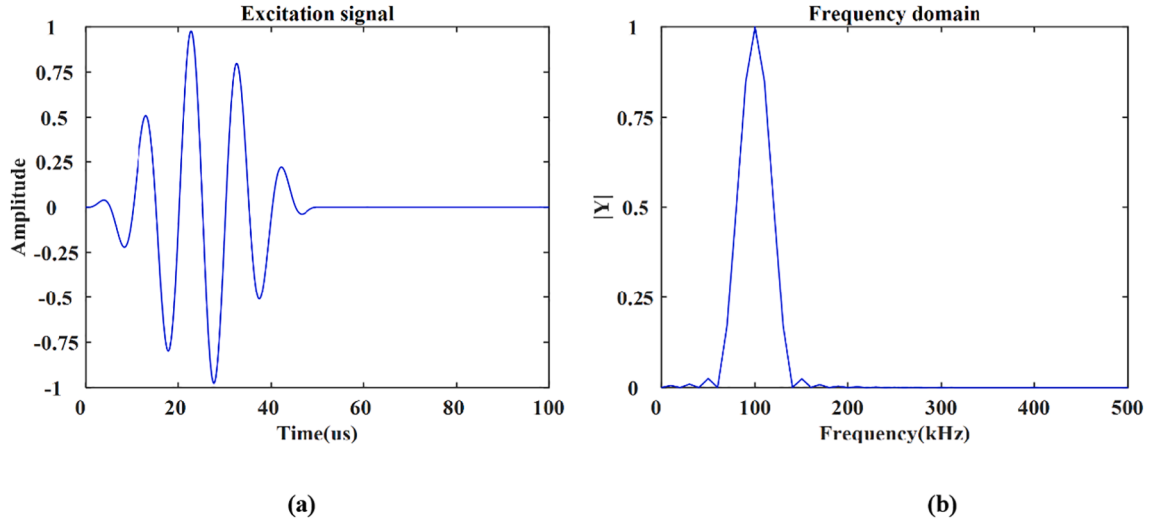


Fig. 4. Excitation signal: (a) in the time domain; (b) in frequency domains.

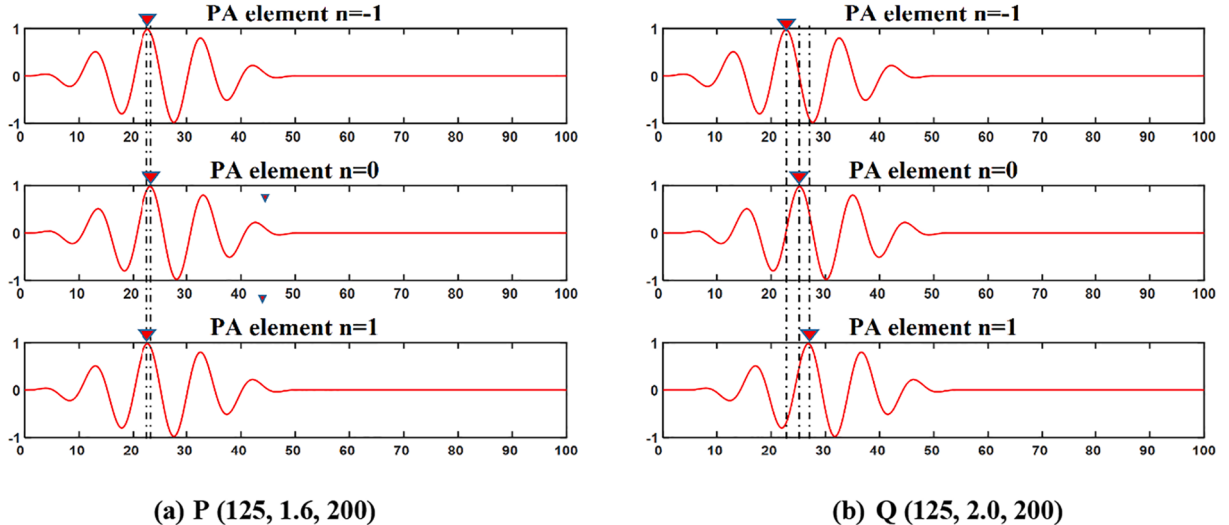


Fig. 5. Time delay calculated by PA theory of curved plate when the focal point at (a) P (125, 1.6, 200);(b) Q (125, 2.0, 200).

should meet the CFL condition [44]:

$$\Delta t \leq \frac{L_{\min}}{c_L} \quad (22)$$

$$\Delta t \leq \frac{1}{20f_{\max}} \quad (23)$$

where L_{\min} is the element size and c_L is the longitudinal velocity. Therefore, the time step was set to 2.5×10^{-8} s, while the total simulation time was 0.5 ms.

A five-cycle sinusoidal tone-burst signal enclosed in a Hanning window is chosen as the basic excitation signal, as shown in Fig. 4, in both time and frequency domains, which is prescribed at active PA (loading nodes) to generate the guided waves. The center frequency of the signal is selected to be 100 kHz to excite both CLT_0 and CLT_1 modes but ensure that the modes are separable in the recorded signals due to the difference in their group velocities. With this setup, the two modes will be easier to distinguish from the back-scattered waves generated by damage. The excitation signal is defined as:

$$x(t) = \frac{1}{2} \left(1 - \cos \frac{2\pi f_c t}{k} \right) \sin(2\pi f_c t) \quad (24)$$

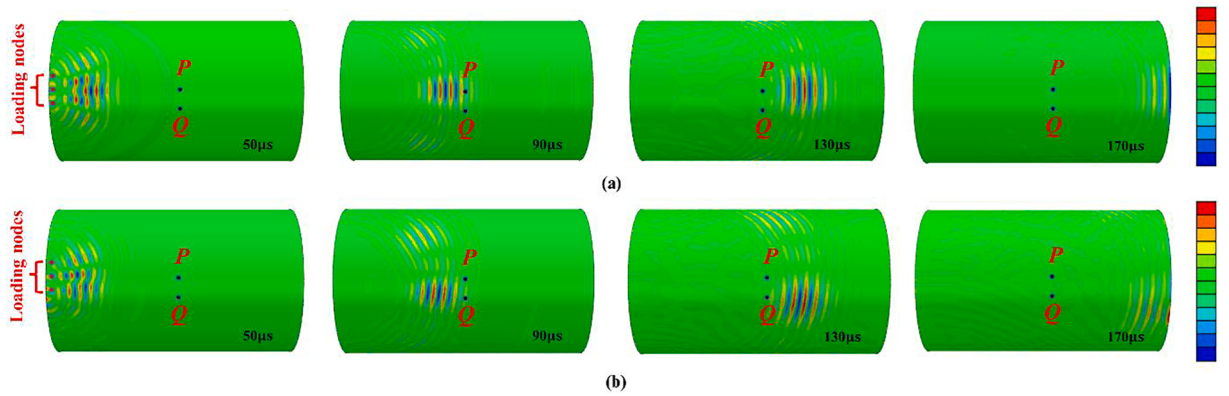


Fig. 6. Wavefield in an undamaged curved plate with a radius of 125 mm when the focal point is at (a) P (b) Q.

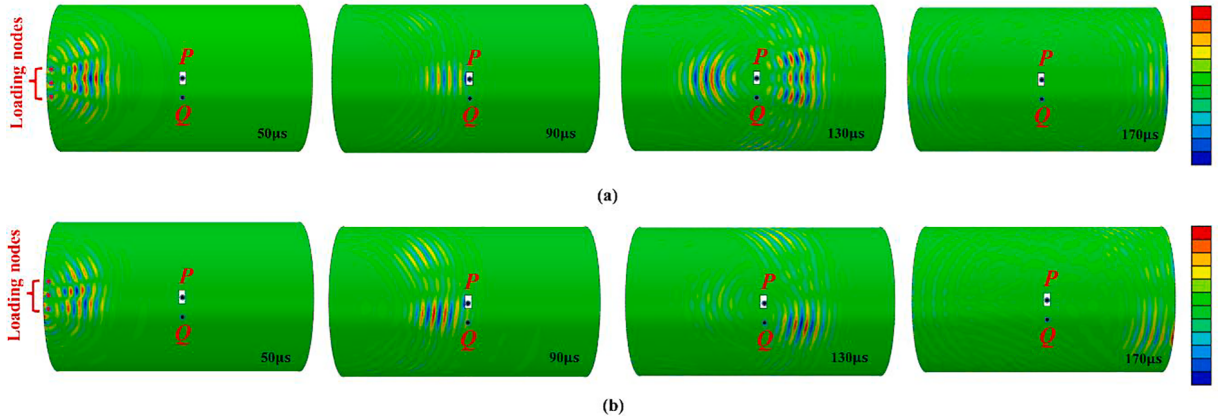


Fig. 7. Wavefield in a damaged curved plate with a radius of 125 mm when the focal point is at (a) P (b) Q.

where $t \leq k/f_c$, f_c is the center frequency of the sine wave, k is the number of cycles of the sinusoidal signal, and $k = 5$.

To study the effect of curvature radius, six curved plates are considered which are thin aluminum alloy 6061 plates 40 cm by 40 cm in the area with a thickness of 4 mm and radii of 125 mm, 250 mm, 500 mm, 1000 mm, and 5000 mm.

3.2. PA focusing

To observe the focusing capabilities of the PA using numerical simulation, a curved plate with a radius of 125 mm in a pristine (undamaged) condition is considered. The plate is excited via the active PA targeting the focal points P (125, 1.6, 200) and Q (125, 2.0, 200) (viz. Fig. 6). Based on the prescribed excitation signal, the PA focusing theory calculates the necessary activation time delay between each successive loading node to target the desired focal points. For example, to achieve the first focal point P (125, 1.6, 200), the time delay between adjacent active PA in the array is 0, 0.5, and 0 μs. To achieve the second focal point Q (125, 2.0, 200), the time delay is 0, 2.5, and 4.1 μs, just as Fig. 5 shows. Fig. 6 shows the out-of-plane wavefield in the plate at four instances in time. As shown in Fig. 6 (a), from 50 μs to 90 μs, the out-of-plane wavefield is all summed; the summed wavefields clearly show the propagation direction. It can also be seen from Fig. 6 (a), at the moment of 90 μs, that the wavefield is propagating with its energy concentrated at the focal point P, 20 cm from the PA. When the wavefield propagates past the focal point P, at the moment of 130 μs, it disperses before hitting the plate boundary. Around 170 μs, the wavefield after dispersion reaches the boundary. In Fig. 6(b), it is obvious that the propagation direction of the wavefield has shifted to the right towards Q. The wavefield is most concentrated when it is close to the focal point Q. After passing through the focal point Q, the wavefield disperses, and the energy dies down by the time it reaches the boundary.

To simulate damage in the curved plate, rectangular puncture damage with a size of 20 mm by 10 mm by 4 mm is cut in the middle of the curved plate. Similar to the simulation on the pristine curved plate, the active PA is programmed to focus on P (125, 1.6, 200) and Q (125, 2.0, 200). Fig. 7 also provides a plot of the guided wavefield at four instances at a time identical to that of Fig. 6. However, as evident from Fig. 7 (a) at 130 μs, there is a strong interaction between the propagating wavefield and the damage. The damage in the plate generates a strong back-scattered wave that is detected by the passive PA (displacement nodes). The recorded signal can be

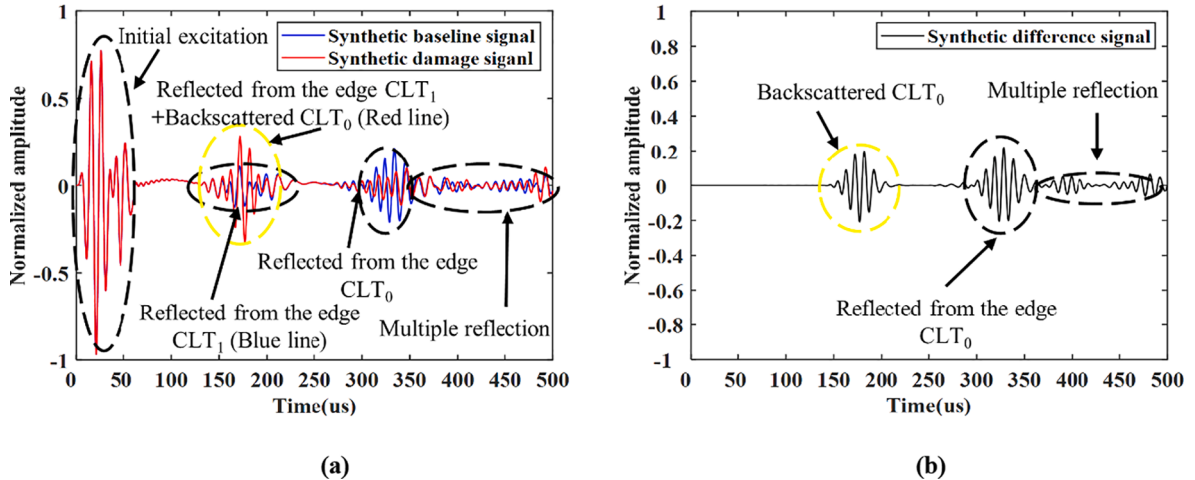


Fig. 8. (a) Synthetic signals of passive PA in both undamaged (baseline) and damaged curved plates with a radius of 125 mm; (b) Difference between the damage signal and baseline signal.

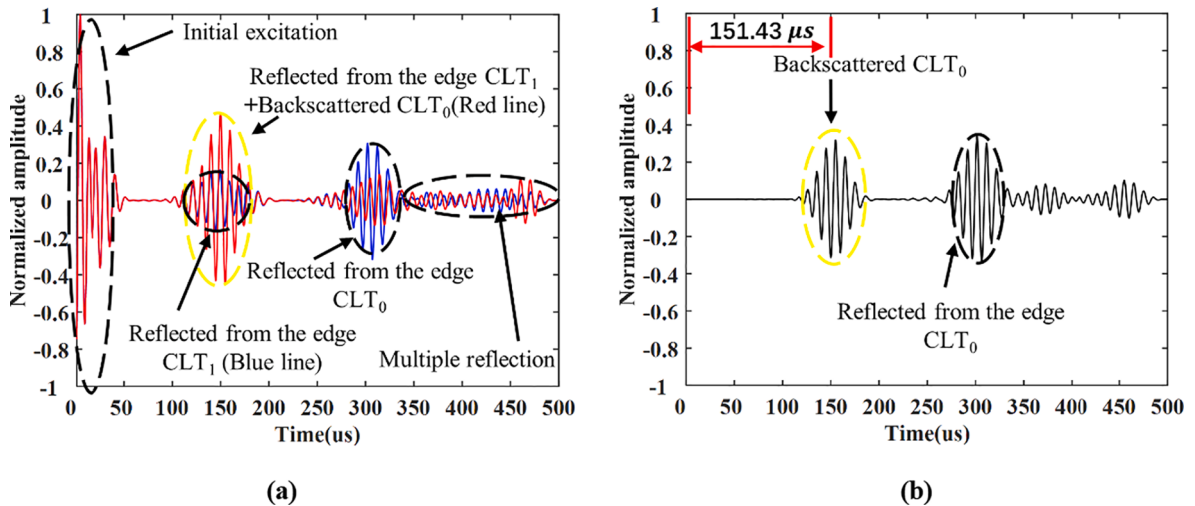


Fig. 9. (a) Synthetic signals of passive PA and calculated after cross-correlation in both undamaged (baseline) and damaged curved plates with a radius of 125 mm; (b) Difference between the damage signal and baseline signal.

processed by applying the PA damage localization theory, and the location of the damage can be determined. On the other hand, when the PA guided wave focuses on Q (125, 2.0, 200), from Fig. 7(b) at 130 μs, we can see that the interaction between the damage and the wavefield is minimal. The back-scattered wave reflected from the damage is hardly detected.

3.3. Damage detection and localization

The PA guided wave properties are studied in the mentioned pristine and damaged curved plate models. The CLT₀ and CLT₁ modes should exist in the wavefield and reflect from the damage and the plate's edge at different times according to their distinct group velocities.

Synthetic signals of passive PA in the damaged and pristine curved plates in response to the same excitation are plotted in Fig. 8. Synthetic signals refer to the superimposition of the received signals through the PA damage localization theory. Synthetic signals are normalized by the amplitude with the largest absolute value. As shown in Fig. 8(a), CLT₀ and CLT₁ modes are evident in the initial excitation and the reflection from the edge of both plates. However, in the synthetic signal of the damaged plate, the CLT₀ back-scattered from the damage is also present. To better isolate the back-scattered CLT₀, the signal of the pristine curved plate (synthetic baseline signal) is subtracted from that of the damaged curved plate. The synthetic difference signal is plotted in Fig. 8(b). The synthetic difference signal will not contain any effects from damage attributed to plate manufacturing, solely from post-manufacturing damage. This yields a more reliable signal for damage assessment. For the CLT₁ mode, combined with the group velocity of CLT₁ and

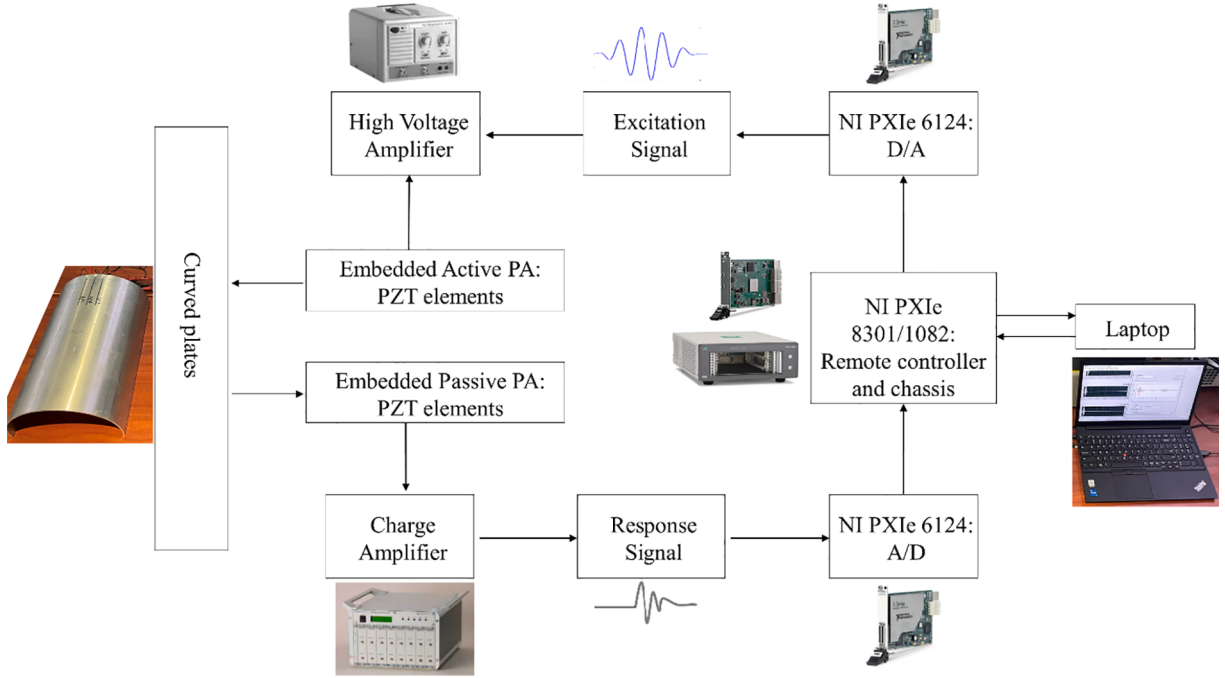


Fig. 10. The experimental system scheme.

the location of the damage, we can calculate that the back-scattered CLT₁ should appear roughly in the 70 to 100 μs period. However, it cannot be detected, which shows that CLT₁ is not sensitive to damage. Therefore, in the following, we rely on the back-scattered CLT₀ as the main indicator of damage.

To assess the time of flight (ToF) of each mode, the cross-correlation function, $R_{xy}(\tau)$, is used:

$$R_{xy}(\tau) = \int_{-\infty}^{\infty} x(t) \cdot y(t + \tau) dt \quad (25)$$

where τ is the time lag between signals $x(t)$ and $y(t)$. The initial excitation signal and the reflected waveforms identified as CLT₀ and CLT₁ modes are segmented with the cross-correlation function calculated for varying time lags. The time lag where $R_{xy}(\tau)$ is maximized and is considered the ToF of the mode waveform. The cross-correlation of the synthetic signals and the excitation signal were also calculated and plotted in Fig. 9. Using the group velocities of the CLT₀ mode, the location of the damage relative to the PA can be determined from the ToF of the back-scattered wave. The synthetic difference signal after cross-correlation can be gained using subtraction. The ToF of the back-scattered CLT₀ was determined as 151.43 μs (viz. Fig. 9 (b)). Based on the CLT₀ mode group velocity, the damage location should be 20.94 cm. Contrastingly, the real distance between the PA and the center of the damage is 20 cm. Therefore, the error in damage localization was 4.71 % which is very close to the results of the existing literature [45]. Thus, the method proposed in this study has the capability of damage identification in the curved plate.

4. Laboratory study

To verify the numerical simulations, a data acquisition system for PA guided wave SHM is built in the laboratory, and an experimental study is carried out on a pristine and damaged curved plate with a radius of 125 mm.

4.1. Data acquisition system for PA guided wave SHM

The vast majority of PA approaches adopt a synthetic aperture strategy where piezoelectric elements in the PA are operated individually, and pulses are set off in a round-robin fashion [46]. However, in this study, we use parallel PA excitation which offers a much faster inspection ability and reduced postprocessing demands. To achieve this, we need to equip each PZT in the active PA with a high-voltage amplifier to make sure PZT elements were excited simultaneously during the experiment. Theoretically, we can use as many piezoelectric elements as possible to achieve PA focusing. However, due to the practical restraints including equipment availability, we chose to use 3 piezoelectric elements to form the active PA and another 3 piezoelectric elements to form the passive PA. This strategy is adequate to verify the proposed method.

Therefore, a commonly used National Instruments data acquisition system was adopted and expanded to include the capability for PA-based guided wave inspection of structures. This study required a data acquisition card capable of offering high-speed input/output

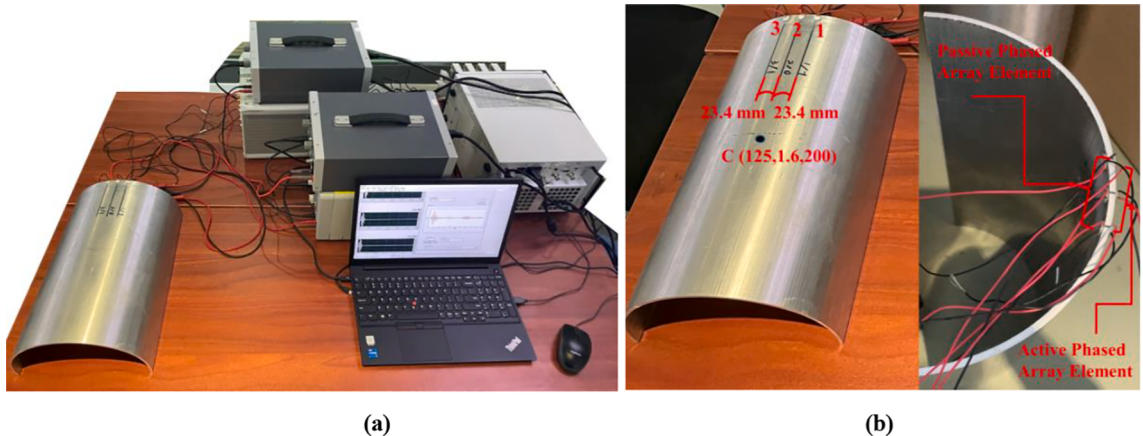


Fig. 11. (a) Hardware and software are developed to detect damages in a curved plate; (b) The set up with measurement lengths annotated and focus point, PZT locations indicated.

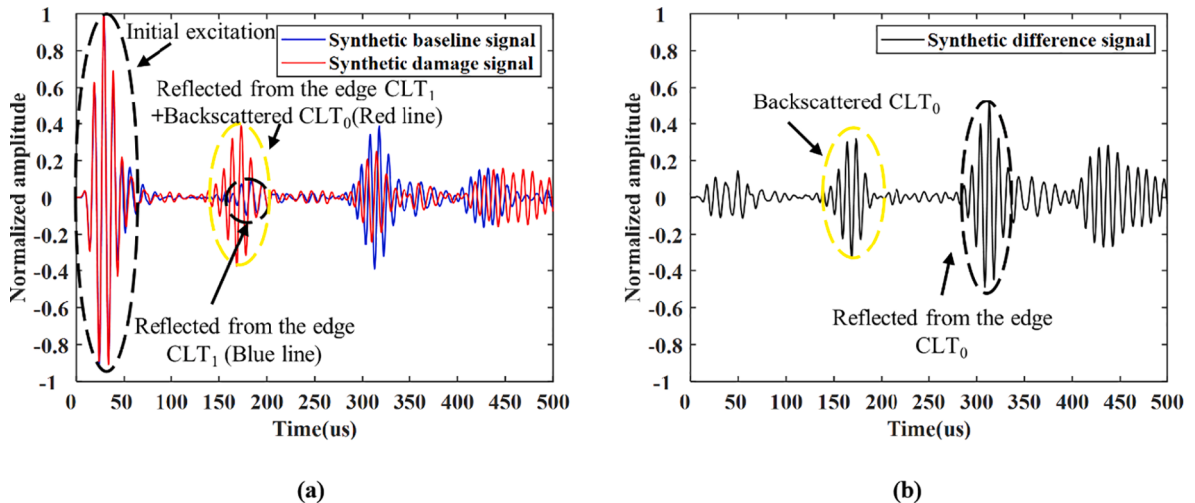


Fig. 12. (a) Synthetic signals of passive PA in both undamaged(baseline) and damaged curved plates with a radius of 125 mm in the experiment; (b) Difference between the damage signal and baseline signal.

sampling in the experiment. Hence, a National Instruments PXIe-1082 chassis was chosen, as it can hold multiple data acquisition cards. Four PXIe-6124 data acquisition cards are installed in the PXIe-1082 chassis to send and receive signals from piezoelectric elements bonded to the surface of the curved plates. The PXIe-6124 has 2 analog output channels and 4 analog input channels. The analog inputs are sampled with 16-bit resolution and with a maximum sampling rate of 4 MHz. This experimental setup offers multiple input and output channels with high-speed sampling rates, which provides the desired versatility to SHM system designers.

On one edge of each plate, an active PA consisting of 3 PZT discs is attached to the upper surface. While a passive PA consisting of 3 PZT discs is bonded to the lower surface of each plate. The PZT discs are bonded to the aluminum plates using cyanoacrylate glue in an arc-linear array. Wires are bonded to the top surface of the elements using copper tape to establish a connection between the PZT discs and the data acquisition system. LabVIEW ensures the time synchronization between all of the input and output channels irrespective of which data acquisition card is generating or measuring signals. It is also used to set up, calibrate, and focus the waveforms emitted from the PA. The high voltage amplifier is used to linearly amplify the excitation voltage signal so that it can drive the active PA. While the charge amplifier is used to convert the charge signal received by the passive PA into a voltage signal. The recorded data are used to locate the damage via further processing.

The experimental system used in this study is shown in Fig. 10. By applying the same, but time-delayed waveform to each element of the active PA, a controllable wavefront can be generated through the superimposition of individual waves. Through superimposition, the individual waves sum to form a wavefront towards the focal point (R, θ, z) . The focal point is at a distance R_f from the center of the PA. By adjusting the time delay between the PZT elements in the PA, the location of the focal point can be varied to scan for potential damage locations.

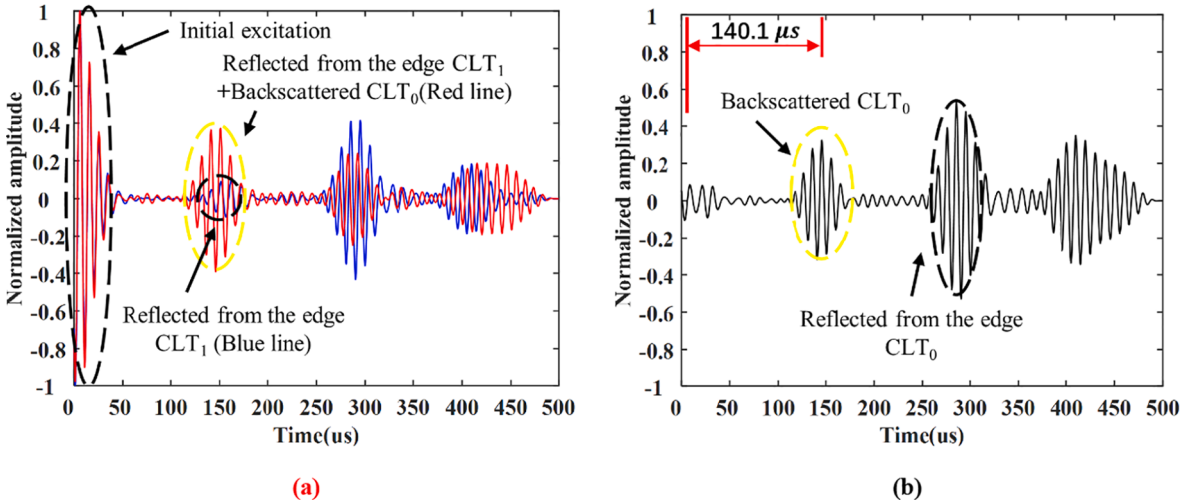


Fig. 13. (a) Synthetic signals of passive PA and calculated after cross-correlation in both undamaged(baseline) and damaged curved plates with a radius of 125 mm in the experiment; (b) Difference between the damage signal and baseline signal.

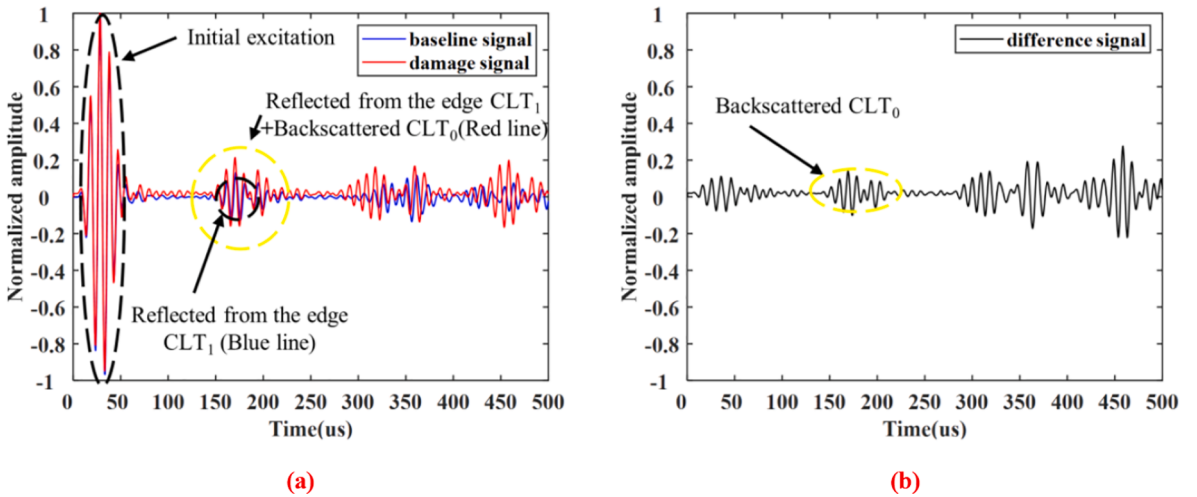


Fig. 14. (a) Received signal of the PZT in both undamaged (baseline) and damaged curved plates with a radius of 125 mm in the supplementary experiment; (b) Difference between the damage signal and baseline signal.

4.2. Experimental method

To validate the numerical simulations, thin 6061 aluminum alloy curved plates with a size of 40 cm by 40 cm by 4 mm and a radius of 125 mm are tested. The material parameters of the aluminum are tabulated in Table 1. In the experiment, we use 3 PZTs discs (1 mm thick and 10 mm in diameter) in each of the active and the passive PA (viz. Fig. 11). The distance between the PZTs elements is 23.4 mm. This distance is chosen to ensure that the time delay between the waves emitted by neighboring PZTs is always an integer multiple of 0.5 μs, which is the minimum sampling interval of the NI PXIE-6124. Signals are generated and collected in the active and passive PA with a sampling rate of 2 MHz.

The active PA and the passive PA are respectively excited and sensed by the high-speed acquisition system which is shown in Fig. 11 (a). The focal point was set at the center of the plate, C (125, 1.6, 200), and the time delays were $x_1 = 0$, $x_2 = 0.5$, and $x_3 = 0 \mu\text{s}$ between PZTs, in turn (viz. Fig. 11 (b)). The excitation signal is the same as the one used in the numerical simulations. To control the three PZT elements in the active PA a total of 3 analog output channels on the data acquisition cards were utilized. The excitation signal of each analog channel calculated by PA focusing theory is powered up to 150 V through the PINTECH high voltage amplifier (one HA-405 and two HA-820). On the other hand, the received charge signals on the passive PA were converted to a voltage signal by the DONGHUA charge amplifier and finally collected by LabVIEW using three analog input channels on a PXIE-6124.

To ensure consistency between tests and eliminate the influence of manufacturing, the synthetic signal of the damaged curved plate is subtracted from the undamaged one. Since the center frequency of the transducer is 100 kHz, a band-pass filter between 30 kHz and

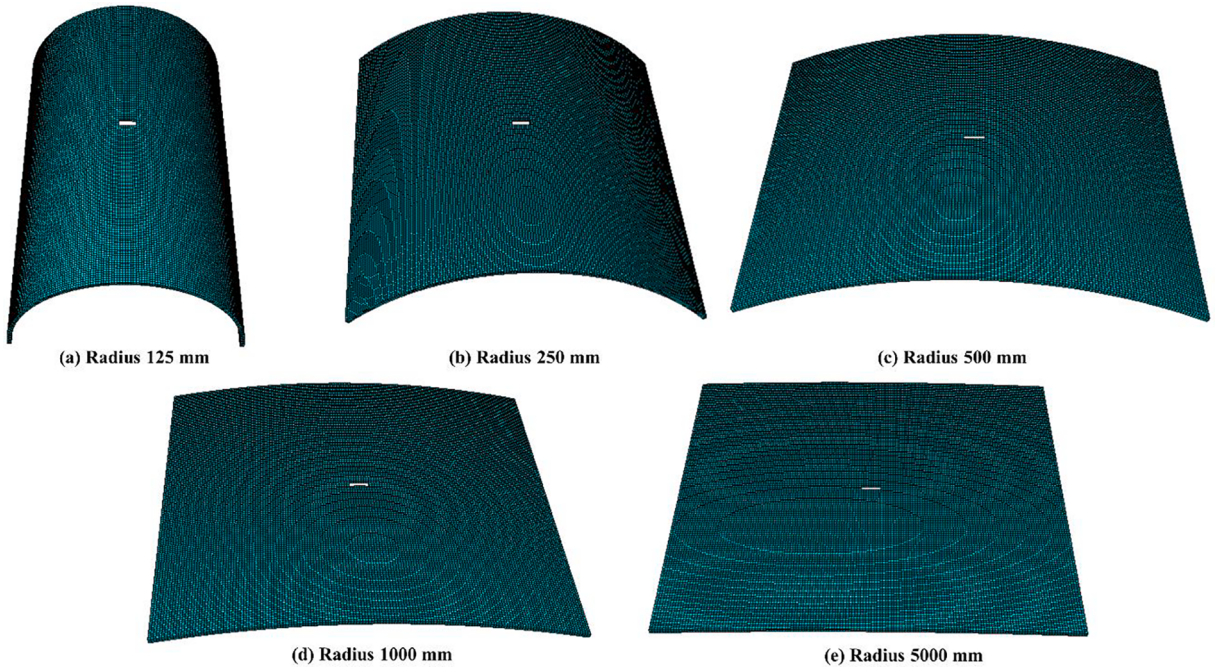


Fig. 15. Models of five different curved plates with puncture damage in their center.

Table 2
Parameters of curved plates with different radii.

Radius [mm]	Material	Width [mm]	Length [mm]	Thickness [mm]	Damage width [mm]	Damage length [mm]	Damage depth [mm]
125, 250, 500,1000, 5000	6061 Aluminum	400	400	4	20	10	4

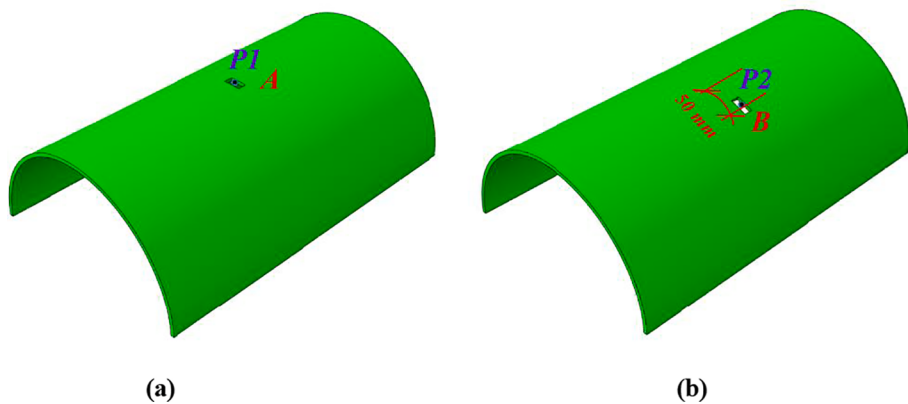


Fig. 16. Focal points and damage location: (a) The focal point $P1$ and Damage A; (b) The focal point $P2$ and Damage B.

300 kHz is applied to the recorded signals to reduce the noise outside the signal bandwidth.

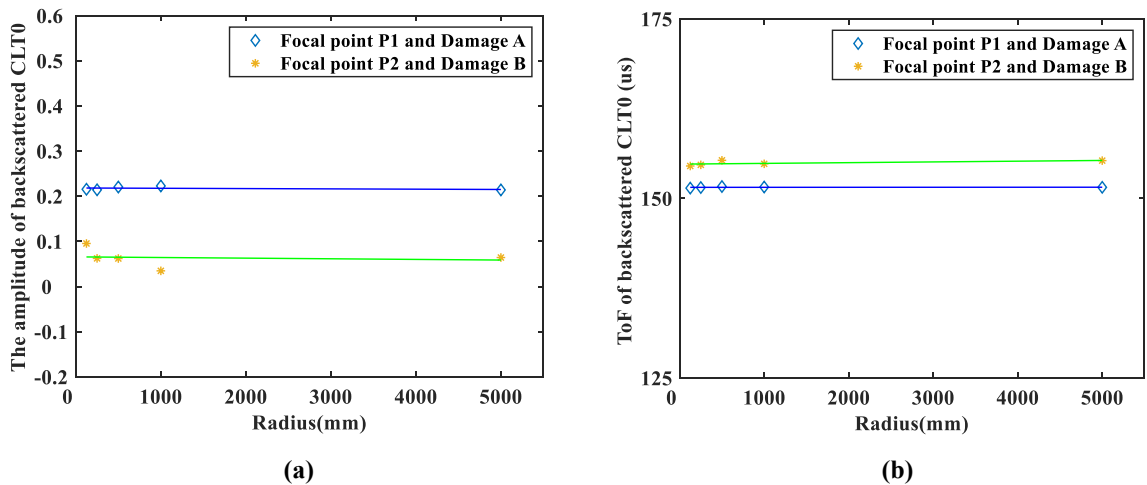
4.3. Experimental result and model verification

Fig. 12 (a) shows synthetic signals for both the pristine and the damaged curved plates. In **Fig. 12** (b), the responses from the damaged curved plate have a strong back-scattered CLT₀ which indicates damage. After calculating the cross-correlation, and comparing it with the excitation signal, the ToF between the excitation source and the back-scattered CLT₀ is 140.1 μ s (viz. **Fig. 13** (b)).

Table 3

Results based on the numerical models with different radii in two damage locations.

Radius [mm]	Focal point coordinates [mm]	Damage center Coordinates [mm]	Damage move distance [mm]	Before cross-correlation analysis The amplitude of backscattered CLT ₀	After cross-correlation analysis ToF of backscattered CLT ₀ [μs]	Predicted damage location [cm]	Damage localization error [%]
125	P1 (125,1.6,200)	A (125,1.6,200)	0	0.22	151.43	20.94	4.7
	P2 (125,2.0,200)	B (125,2.0,200)	50	0.095	154.51	21.37	3.6
250	P1 (250,0.8,200)	A (250,0.8,200)	0	0.21	151.51	20.95	4.8
	P2 (250,1.0,200)	B (250,1.0,200)	50	0.062	154.67	21.39	3.7
500	P1 (500,0.4,200)	A (500,0.4,200)	0	0.22	151.65	20.97	4.9
	P2 (500,0.5,200)	B (500,0.5,200)	50	0.062	155.30	21.48	4.2
1000	P1 (1000,0.2,200)	A (1000,0.2,200)	0	0.22	151.58	20.96	4.8
	P2 (1000,0.205,200)	B (1000,0.205,200)	50	0.035	154.81	21.41	3.8
5000	P1 (5000,0.04,200)	A (5000,0.04,200)	0	0.21	151.54	20.96	4.8
	P2 (5000,0.05,200)	B (5000,0.05,200)	50	0.064	155.26	21.47	4.1

**Fig. 17.** Relationship between radii of the plate and the four parameters for two damage locations: (a) the amplitude of back-scattered CLT₀; (b) ToF of back-scattered CLT₀;

This means that the damage should be located 19.38 cm away from the PZT elements. The real distance is 20 cm, hence the localization error was 3.12 % for this experiment.

To demonstrate the usefulness of PA with 3 elements, another experiment with a single transmitter and receiver in the same plates was implemented. This time we only used the number 2 PZT in active PA and passive PA (viz. Fig. 11 (b)). The results are shown in Fig. 14. Comparing Fig. 14 (b) with Fig. 12 (b), it can be found that the amplitude of the backscattered CLT₀ for the experiment with only a single transmitter and receiver is significantly smaller, around 0.2, while for the experiment with PA it is around 0.4. This indicates that the PA with 3 elements is adequate and can significantly improve the SNR of the backscattered CLT₀, which proves the effectiveness and usefulness of the PA. Furthermore, the results above prove that the herein utilized experimental system is reliable and stable to carry out studies for guided PA wave propagation.

To verify the finite element curved plate models, the experimental results of PA can be compared with the simulation results. Comparing Fig. 13 (b) and Fig. 9 (b), obvious back-scattered CLT₀ can be found in both cases. Their amplitudes are all around 0.4, their ToF is also very close, and the difference between the errors in the two damage localizations is only 1.6 %. This shows that the proposed PA method is effective to analyse the PA guided wave propagation in finite element models.

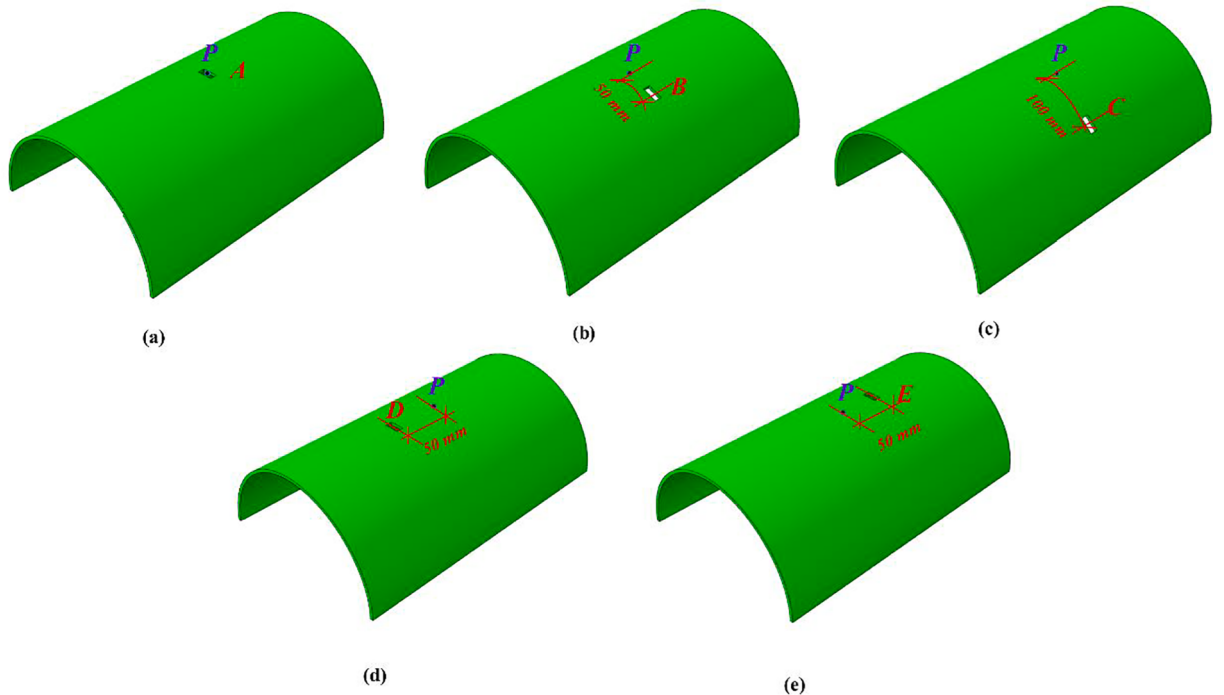


Fig. 18. For plates with a radius of 125 mm, five different damage locations:(a) Damage A (b) Damage B (c) Damage C (d) Damage D (e) Damage E.

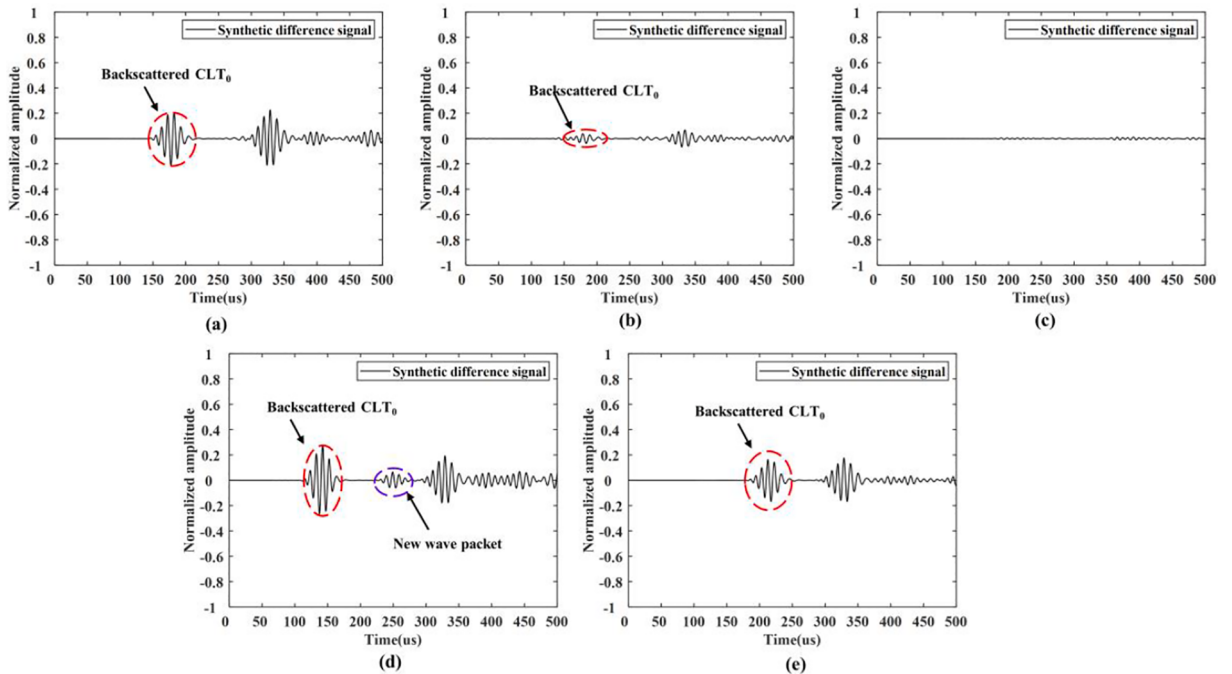


Fig. 19. Synthetic difference signal of plates with a radius of 125 mm in five different damage locations: (a) Damage A (b) Damage B (c) Damage C (d) Damage D (e) Damage E.

5. Parametric study

To study the feasibility of the PA guided wave method and the behavior of PA guided wave propagation in curved plates in various conditions, the effect of plate radius, damage location, and damage width are studied using the finite element method.

Table 4

Results based on the numerical models with different radii in different damage locations.

Radius [mm]	Focal point coordinate [mm]	Damage center Coordinates [mm]	Damage move distance [mm]	Before cross-correlation analysis		After cross-correlation analysis ToF of backscattered CLT ₀ [μs]	Predicted damage location [cm]	Damage localization Error [%]
				The amplitude of backscattered CLT ₀	The amplitude of the new wave packet			
125	P (125,1.6,200)	A (125,1.6,200)	0	0.22	—	151.43	20.94	4.7
		B (125,2.0,200)	50	0.010	—	151.84	21.00	1.8
		C (125,2.4,200)	100	—	—	—	—	—
		D (125,1.6,150)	50	0.27	0.060	111.70	15.45	3.0
		E (125,1.6,250)	50	0.19	—	181.93	25.16	0.6
250	P (250,0.8,200)	A (250,0.8,200)	0	0.21	—	151.51	20.95	4.8
		B (250,1.0,200)	50	0.013	—	143.25	19.81	3.9
		C (250,1.2,200)	100	—	—	—	—	—
		D (250,0.8,150)	50	0.28	0.058	111.46	15.41	2.7
		E (250,0.8,250)	50	0.17	—	181.74	25.13	0.5
500	P (500,0.4,200)	A (500,0.4,200)	0	0.22	—	151.65	20.97	4.9
		B (500,0.5,200)	50	0.015	—	151.55	20.96	1.7
		C (500,0.6,200)	100	—	—	—	—	—
		D (500,0.4,150)	50	0.27	0.065	111.70	15.45	3.0
		E (500,0.4,250)	50	0.17	—	181.87	25.15	0.6
1000	P (1000,0.2,200)	A (1000,0.2,200)	0	0.22	—	151.58	20.96	4.8
		B (1000,0.205,200)	50	0.017	—	151.75	20.99	1.8
		C (1000,0.21,200)	100	—	—	—	—	—
		D (1000,0.2,150)	50	0.27	0.068	111.54	15.43	2.9
		E (1000,0.2,250)	50	0.16	—	181.75	25.14	0.6
5000	(5000,0.04,200)	A (5000,0.04,200)	0	0.21	—	151.54	20.96	4.8
		B (5000,0.05,200)	50	0.011	—	152.47	21.09	2.3
		C (5000,0.06,200)	100	—	—	—	—	—
		D (5000,0.04,150)	50	0.26	0.069	111.44	15.41	2.7
		E (5000,0.04,250)	50	0.16	—	181.98	25.17	0.7

5.1. The effect of the inspected plate's radius on the PA guided wave.

To study the effect of curvature, six curved plates were considered with a radius of 125 mm, 250 mm, 500 mm, 1000 mm, and 5000 mm. For each radius, a plate with the damage at its axial center (Damage A) and one with the damage moved 50 mm circumferentially from its center (Damage B) is created. This variation of damage position is used to verify the identification performance of the proposed PA method for damage in the axial or circumferential position. Fig. 15 shows the meshed FEM models for each curved plate with the damage located at the center. More details are shown in Table 2. The focal point of the PA guided wave is always set at the center of the damage (P_1, P_2) (viz. Fig. 16). This means that if the damage is in the center of the plate, the distance from it to the PA is 20 cm. If the damage moves 50 mm circumferentially from the center of the plate, then the distance from it to the PA is 20.6 cm.

For the plate with a radius of 125 mm and damage located at the center, the synthetic baseline (pristine plate's response) and damage signals captured by the passive PA during guided wave propagation are shown in Fig. 8, which plots the normalized signal amplitudes versus time. Fig. 8 indicates the wave modes analysis results. Therefore, for plates with other radius and damage locations, the wave modes can be analyzed in the same way and the results are summarized in Table 3.

Fig. 17 shows the relationship between the two parameters and the radius of the plate for two damage locations. Fig. 17 (a) shows the amplitude of back-scattered CLT₀ for the two damage locations in the curved plates. In this figure, one can see that with the increase of the plate radius, when the damage is in the axial center (Damage scenario A), the amplitude of back-scattered CLT₀ without significant change. When the damage moves from the center to the circumference (Damage scenario B), the reflected wave amplitude is also generally linear, although there are some small changes. This is because the energy of the guided wavefield is concentrated on the focal point, if the damage is in the axial center, it can propagate straight along the central axis of the plate to the boundary. Therefore, changing the radius has almost no effect on the waveforms. However, if the damage is moved perpendicular to the central axis of the curved plates since the PA guided wave propagates to the lateral boundary, the back-scattered CLT₀ will be more likely to be affected by the boundary reflected wave. This also explains why the amplitude of back-scattered CLT₀ in Damage scenario B is smaller than that in Damage scenario A. Fig. 17 (b) shows the ToF of backscattered CLT₀ is not sensitive to the change of the radius of the plate for both Damage scenario A and Damage scenario B. According to Table 3, all the damage localization errors are less than 5 %. We can conclude

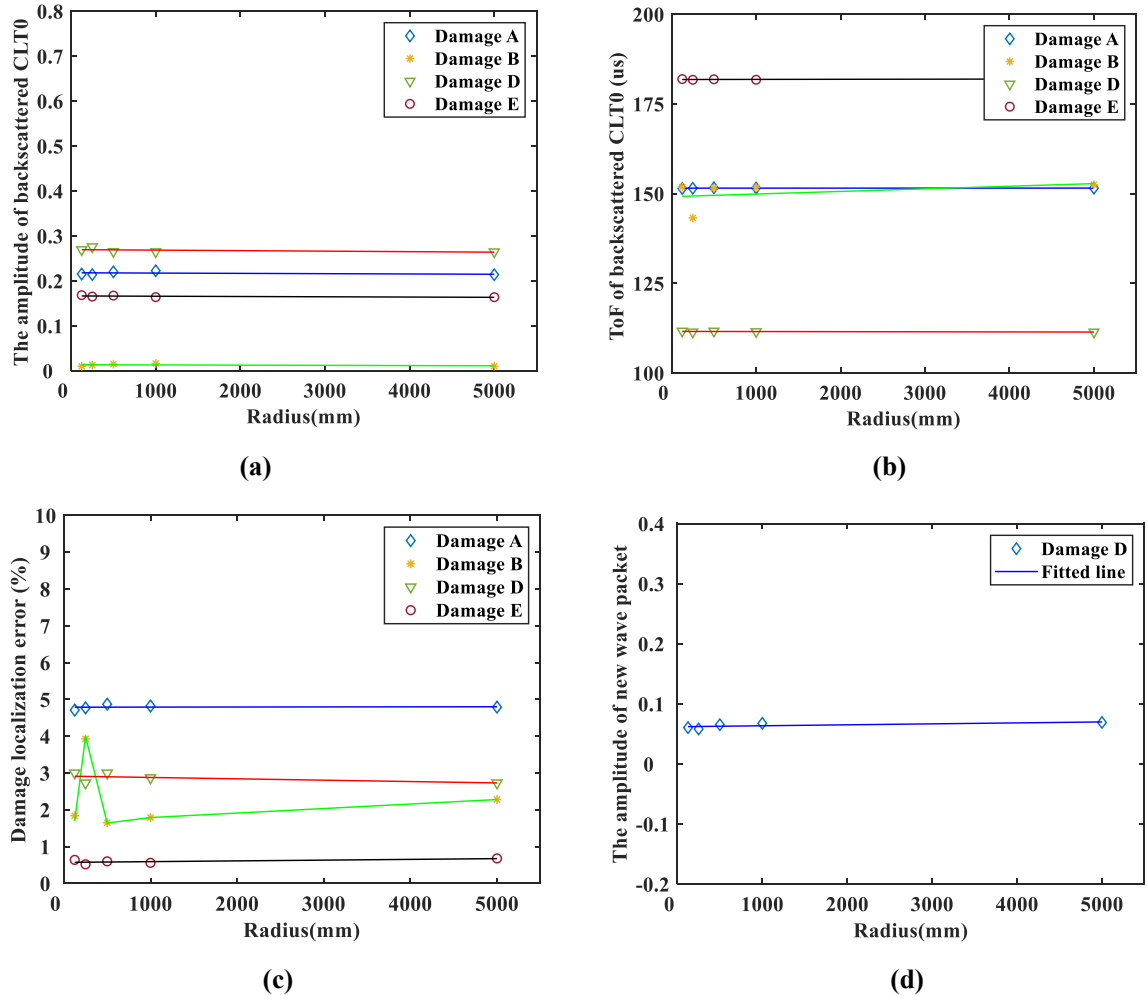


Fig. 20. Relationship between the radius of the plate and the four parameters for different damage scenarios: (a) the amplitude of back-scattered CLT₀; (b) ToF of back-scattered CLT₀; (c)Damage localization error; (d) the amplitude of new wave packet.

that the proposed PA method can detect and locate damage in both the axial and the circumferential directions of a curved plate.

5.2. The effects of damage location on PA guided wave

To investigate the effect of damage location on PA guided wave, plates with five damage positions A, B, C, D, and E were modelled with various radii, as described in the previous section. For plates with a radius of 125 mm, five different damage locations are shown in Fig. 18. The same is true for plates with other radii, although the coordinates of the damage and focal point will change as the radius changes. In this section, to limit the variation, the focal point is always set at the center of the plate.

For plates with a radius of 125 mm and five different damage locations, the synthetic difference signals are shown in Fig. 19. This figure also indicates the wave mode analysis results. It can be seen from Fig. 19 that when the damage gradually moves to the circumferential direction and away from the focal point (fixed at the axial center of the plate), the amplitude of back-scattered CLT₀ decreases rapidly, and there is no obvious back-scattered CLT₀ damage wave in Damage C. When the damage is in front of the focal point (Damage D), although the amplitude of back-scattered CLT₀ increases, an obvious new wave packet appears. The ToF of this new wave packet (around 250 μ s) is about twice the ToF of the backscattered CLT₀ (around 130 μ s). Thus, this new wave packet is regarded as the reflection of the first backscattered CLT₀ on the left edge of the plate. For Damage scenario A, the travel distance for the new wave packet is twice the plate length. Therefore, it arrives simultaneously with the backscattered CLT₀ from the right edge of the plate. This is also almost the case for the E. For Damage scenarios B and C, the amplitude of the first backscattered CLT₀ is very small, and thus the reflections are negligible. When the damage is behind the focal point (Damage E), the amplitude of back-scattered CLT₀ slightly decreases. For the plates with other radii, the wave modes were analyzed in the same way and the results are summarized in Table 4. In Table 4, the localization error for Damage scenario B is always lower than that of Damage scenario A. This is because, for Damage scenario B, the actual damage location from the PA center to damage B can be calculated by using the squared root of a distance of 200

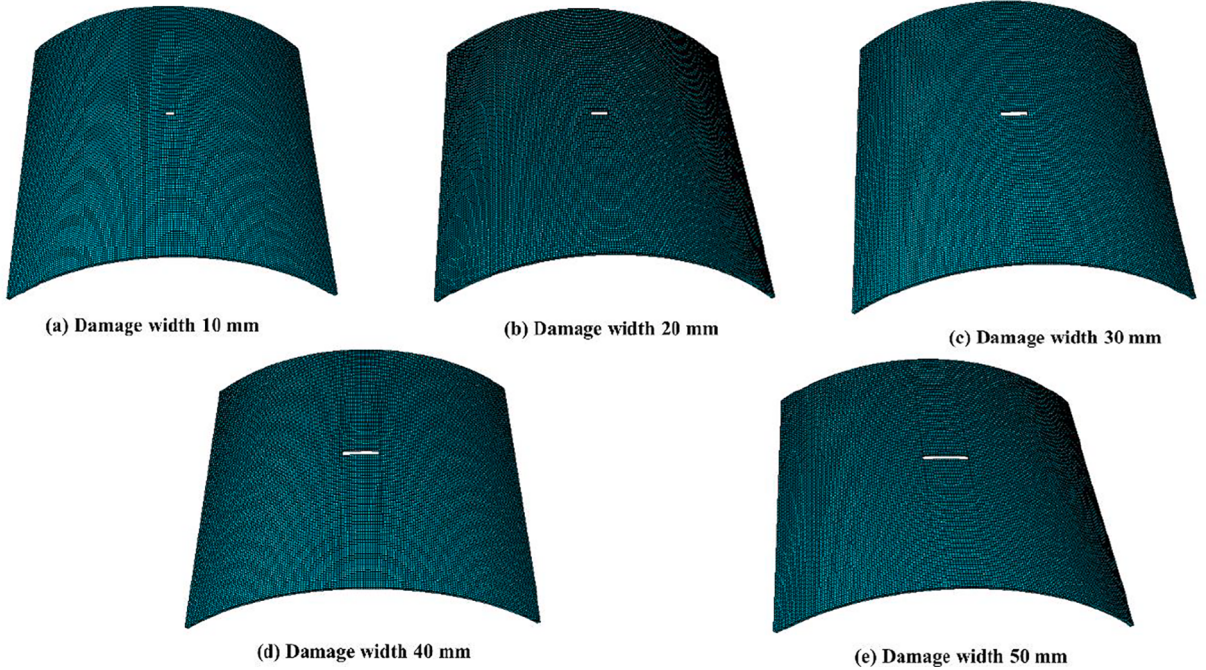


Fig. 21. Models of plates with different damage widths.

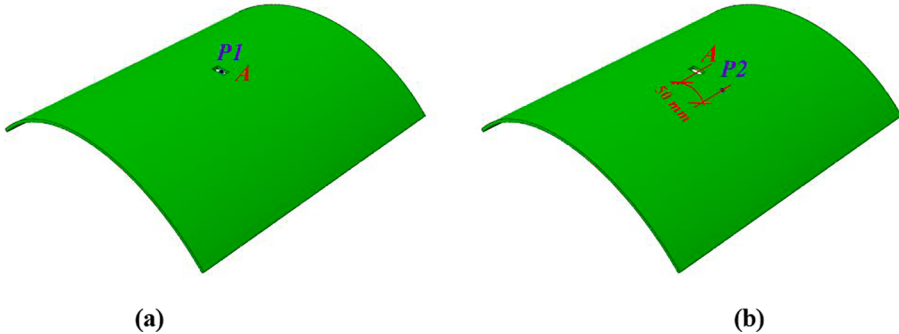


Fig. 22. For plates with a radius of 250 mm, two focal point locations: (a) P1 and (b) P2.

mm (the distance from the focal point to the actuator) and 50 mm (the distance of the damage deviates from the focal point). This result is different from the previously considered 20 cm, for Damage scenario A.

Fig. 20 shows the relationship between four parameters and the radius of the plate for different damage locations. Fig. 20 (a) shows the amplitude of back-scattered CLT₀ of five different damage locations for curved plates with increasing radii. In this figure, we can see that with the increase of the plate radius, the amplitude of back-scattered CLT₀ remains virtually unchanged. Damage A, D, and E are damages located in line with the focal point, which means that the PA guided wave will pass directly through them. Damage B and C, are located far from the PA guided wave propagation path. As can be seen from Fig. 20 (a), for Damage A, D, and E, the amplitude of the back-scattered CLT₀ remains approximately the same for all radii as shown by the three horizontal lines. For Damage B, the back-scattered CLT₀ becomes very small due to its distance from the focal point. While, for Damage scenario C, there is no observed back-scattered wave. For Damage scenario B in Fig. 20 (b), when the radius is 250 mm, its ToF is significantly different than plates with other radii. This is due to the reading error when picking the moment corresponding to the maximum amplitude caused by the extremely small and inconspicuous back-scattered CLT₀ wave, which also causes the peak seen in Fig. 20 (c). In Fig. 20 (c), it can be found that all errors are below 5 %, which also proves the effectiveness of the proposed PA method. An interesting thing is that in the scenario of damage D for each radius, a new wave packet was found, which is almost invariant with radius change.

Considering Fig. 20 (a), (c), and (d), it can be found that for Damage D, although the damage localization error is better and the amplitude of back-scattered CLT₀ is greater than that for Damage A, the new wave packet is generated that interfere with the signal. For Damage E, although the localization error is the smallest, the amplitude of back-scattered CLT₀ is smaller than that of Damage A.

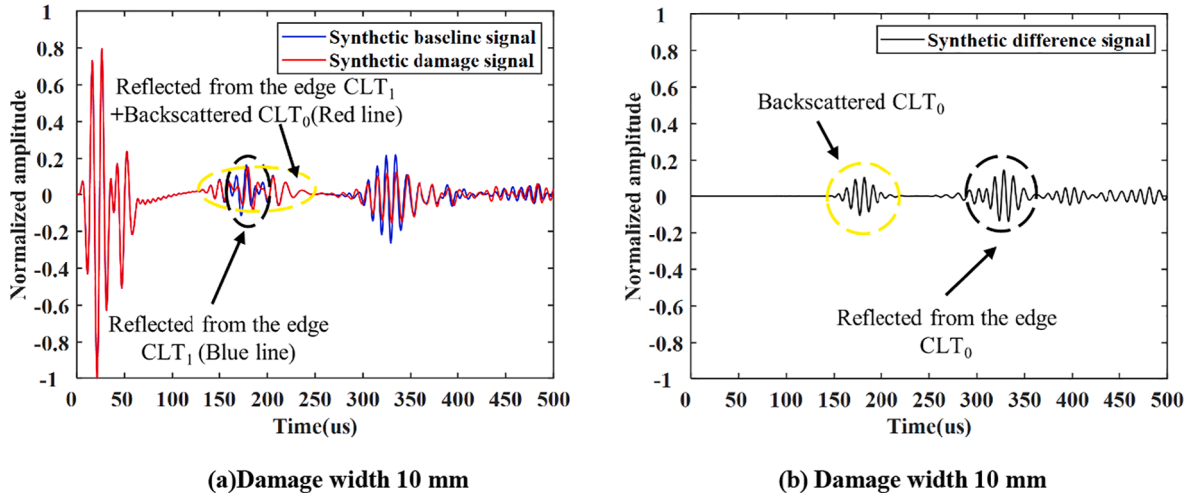


Fig. 23. (a) Synthetic signals of passive PA in both undamaged(baseline) and damaged curved plates with a damage of 10 mm width; (b) Difference between the damage signal and baseline signal.

Table 5

Results based on the numerical models with different damage lengths in different focal points.

Radius [mm]	Focal point coordinate [mm]	Damage center coordinate [mm]	Damage width [mm]	Before cross-correlation analysis		Predicted damage location [mm]	Damage localization error [%]
				The amplitude of backscattered CLT ₀	After cross-correlation analysis ToF of backscattered CLT ₀ [μs]		
250	P1 (250,0.8,200)	A (250,0.8,200)	10	0.10	150.53	20.82	4.1
			20	0.21	151.51	20.95	4.8
			30	0.32	151.59	20.96	4.8
			40	0.34	151.64	20.97	4.9
			50	0.43	152.06	21.03	5.2
	P2 (250,1.0,200)	A (250,0.8,200)	10	0.048	155.85	21.55	7.8
			20	0.12	157.06	21.72	8.6
			30	0.21	157.28	21.75	8.8
			40	0.33	157.55	21.79	9.0
			50	0.41	158.15	21.87	9.4

The localization error in Damage scenario A is the highest, however, it remains within the allowable range. The results show that the proposed PA method allows for wave focusing and can identify damage locations. From the above observations, we can derive some tips for a potential damage localization method that may suit future damage scanning techniques using PA elements. If there is no back-scattered CLT₀, it means that the damage is not on the propagation path of the PA guided wave, and the radian coordinate of the focal point needs to be changed. As long as the damage is in the path of the PA guided wave, the proposed method can identify its location.

5.3. Damage width effects on PA guided wave

To investigate the effects of damage size, another five models with different damage widths were constructed. Fig. 21 shows the meshed FEM models. In these tests, the damage was located at the center of the plates, and two focal points were defined to explore the effect of damage width changes on waveforms under different PA guided wave propagation paths (viz. Fig. 22). The reflected waveforms recorded by the passive PA are plotted in Fig. 23, figure (a) and (b) indicate the wave modes while the rest of the results were summarized in Table 5.

Fig. 24 shows the relationship between the different damage widths and the two parameters for two focal points. From Fig. 24 (a), we can see that the amplitude of the back-scattered CLT₀ significantly increases with the increase of damage width. It's reasonable since the damage acts as an obstacle to the guided wave and causes mode conversion, when the damage width gradually increases, the main part of the CLT₀ mode is reflected by the damage. This leads to an increase in the amplitude of back-scattered CLT₀. However, for the scenario of focal point P1 and Damage A, the increase of the reflected wave amplitude is not completely linear. A possible reason is that the interaction between the PA guided wave and the damage becomes complicated causing more portions of the PA guided wave might be reflected at two lateral boundaries of the plate.

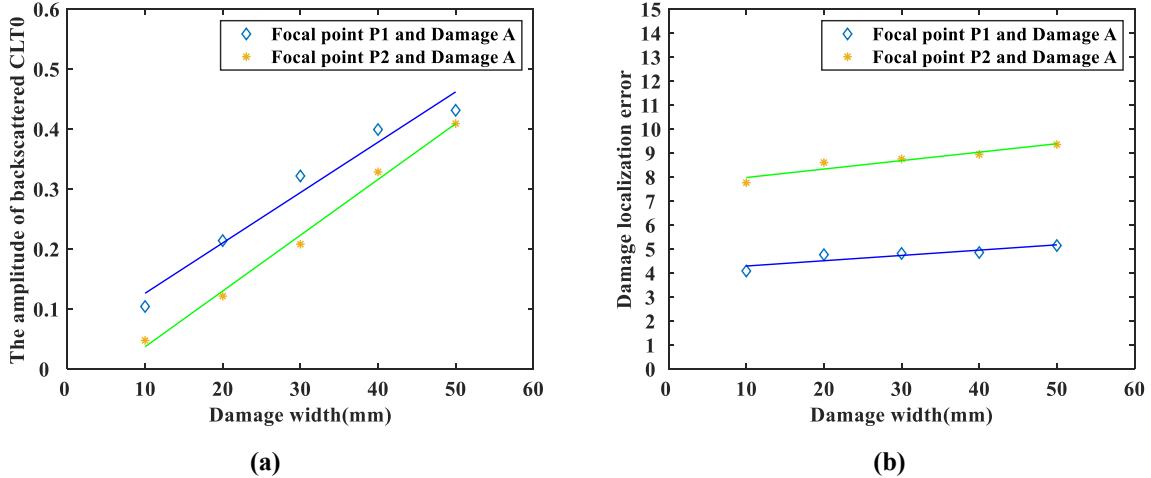


Fig. 24. Relationship between the different damage widths and the two parameters for two focal points: (a) the amplitude of backscattered CLT₀; (b) damage localization error.

As stated in the previous sub-section, when the damage deviates from the PA guided wave propagation path, the amplitude of the back-scattered CLT₀ decreases rapidly. Fig. 24 shows that for the case with focal point P2 and Damage A, when the damage width increases, the amplitude of the back-scattered CLT₀ also increases. However, it always remains smaller than for the cases where the focal point P1 is right on Damage A. This is logical, when Damage A is widened, the focal point P2 moves closer to Damage A, but never as close as P1 which is right inside the Damaged A area. This explains the phenomenon seen in Fig. 23 (a), where the two fitted lines gradually get closer to one another as the damage width increases. From Fig. 23 (b), it can be observed that the accuracy of damage location decreases with the increase of the damage width, no matter whether the focal point is on the damaged area or not. This is because, as the damage width increases, the interaction between the guided wave and the damage becomes more complex, making it more difficult to locate the damage. We deduce from Fig. 23 that when the damage is widened, the back-scattered CLT₀ becomes more evident, but the damage cannot be located with the same degree of accuracy.

6. Conclusion

In this paper, a PA focusing and damage localization method was proposed for the monitoring of curved plates. To analyze the PA guided wave propagation behaviors, finite element models were constructed. A high-speed signal generation and acquisition system was set up for a laboratory study to verify the finite element models. The PA guided wave propagation behaviors corresponding to curved plates with different radii, different damage locations, and sizes were analyzed via the numerical models. According to specific changes in the wave propagation properties, different conclusions were drawn, especially the information about damage location and damage size, given the locations of the PA actuators and sensors. The main contributions are summarized as follows:

- (1). The relationships between the curved plate and the PA guided wave parameters have also been obtained and they can be used to identify the damage in curved plates. The amplitude of back-scattered CLT₀ was proposed as an indicator for existing damage. Based on the ToF of the back-scattered CLT₀, the damage location can be estimated rather accurately.
- (2). Two scenarios were defined to represent axial and circumferential damage on curved plates with different radii. The stability of propagation properties suggested that different radii have almost no effect on the proposed PA method. Moreover, this method can identify damage locations in both the axial and circumferential directions of a curved plate.
- (3). Five different locations of the damage relative to the focal point (of the PA guided wave) were defined to describe scenarios where the focal point is not at the location of the damage. When the damage gradually moves to the circumferential direction and away from the focal point (fixed at the axial center of the plate), the amplitude of back-scattered CLT₀ decreases rapidly. When the damage is in front of the focal point, although the amplitude of back-scattered CLT₀ increases, an obvious new wave packet appears.
- (4). From the simulations on the effects of varying damage widths, we have found that the back-scattered CLT₀ is very sensitive to damage size. When the damage is widened, the back-scattered CLT₀ becomes more evident, but the damage localization accuracy is reduced.

In summary, this study provides an effective PA method for the SHM of curved plate structures. The results indicate that this method is effective at wave focusing and damage identification in curved plates with various radii. However, further interdisciplinary research is required to realize automatic scanning in plates with smaller curvatures, with more eccentric damages, and with non-through damages using the proposed PA method. Based on the sensitivity of the back-scattered CLT₀ to damage size, the next step

will be to combine machine learning and the proposed PA method to realize damage quantification.

CRediT authorship contribution statement

Qi Yuan: Conceptualization, Methodology, Investigation, Software, Formal analysis, Data curation, Visualization, Writing – original draft, Writing – review & editing. **Bence Kato:** Resources, Writing – review & editing. **Keqing Fan:** Methodology. **Ying Wang:** Conceptualization, Methodology, Supervision, Funding acquisition, Project administration, Resources, Validation, Writing – review & editing.

Declaration of Competing Interest

The authors declare that they have no known competing financial interests or personal relationships that could have appeared to influence the work reported in this paper.

Data availability

Data will be made available on request.

Acknowledgment

The authors would like to thank Shenzhen Science, Technology and Innovation Commission, China, for the financial support through Grant JCYJ20210324124212034.

Appendix A

$$D(k, \omega) = \begin{bmatrix} \frac{\hat{\omega}}{\kappa^2} \left[J_{\hat{k}-2} \left(\frac{\hat{\omega}}{\kappa} \right) + J_{\hat{k}+2} \left(\frac{\hat{\omega}}{\kappa} \right) - 2(\kappa^2 - 1) J_{\hat{k}} \left(\frac{\hat{\omega}}{\kappa} \right) \right] & \frac{\hat{\omega}}{\kappa^2} \left[Y_{\hat{k}-2} \left(\frac{\hat{\omega}}{\kappa} \right) + Y_{\hat{k}+2} \left(\frac{\hat{\omega}}{\kappa} \right) - 2(\kappa^2 - 1) Y_{\hat{k}} \left(\frac{\hat{\omega}}{\kappa} \right) \right] & i\hat{\omega}^2 \left[J_{\hat{k}-2}(\hat{\omega}) - J_{\hat{k}+2}(\hat{\omega}) \right] & i\hat{\omega}^2 \left[Y_{\hat{k}-2}(\hat{\omega}) - Y_{\hat{k}+2}(\hat{\omega}) \right] \\ \frac{\eta^2 \hat{\omega}^2}{\kappa^2} \left[J_{\hat{k}-2} \left(\frac{\eta \hat{\omega}}{\kappa} \right) + J_{\hat{k}+2} \left(\frac{\eta \hat{\omega}}{\kappa} \right) - 2(\kappa^2 - 1) J_{\hat{k}} \left(\frac{\eta \hat{\omega}}{\kappa} \right) \right] & \frac{\eta^2 \hat{\omega}^2}{\kappa^2} \left[Y_{\hat{k}-2} \left(\frac{\eta \hat{\omega}}{\kappa} \right) + Y_{\hat{k}+2} \left(\frac{\eta \hat{\omega}}{\kappa} \right) - 2(\kappa^2 - 1) Y_{\hat{k}} \left(\frac{\eta \hat{\omega}}{\kappa} \right) \right] & i\eta^2 \hat{\omega}^2 \left[J_{\hat{k}-2}(\eta \hat{\omega}) - J_{\hat{k}+2}(\eta \hat{\omega}) \right] & i\eta^2 \hat{\omega}^2 \left[Y_{\hat{k}-2}(\eta \hat{\omega}) - Y_{\hat{k}+2}(\eta \hat{\omega}) \right] \\ \frac{i\hat{\omega}^2}{\kappa^2} \left[J_{\hat{k}-2} \left(\frac{\hat{\omega}}{\kappa} \right) - J_{\hat{k}+2} \left(\frac{\hat{\omega}}{\kappa} \right) \right] & \frac{i\hat{\omega}^2}{\kappa^2} \left[Y_{\hat{k}-2} \left(\frac{\hat{\omega}}{\kappa} \right) - Y_{\hat{k}+2} \left(\frac{\hat{\omega}}{\kappa} \right) \right] & -\hat{\omega}^2 \left[J_{\hat{k}-2}(\hat{\omega}) + J_{\hat{k}+2}(\hat{\omega}) \right] & -\hat{\omega}^2 \left[Y_{\hat{k}-2}(\hat{\omega}) + Y_{\hat{k}+2}(\hat{\omega}) \right] \\ \frac{i\eta^2 \hat{\omega}^2}{\kappa^2} \left[J_{\hat{k}-2} \left(\frac{\eta \hat{\omega}}{\kappa} \right) - J_{\hat{k}+2} \left(\frac{\eta \hat{\omega}}{\kappa} \right) \right] & \frac{i\eta^2 \hat{\omega}^2}{\kappa^2} \left[Y_{\hat{k}-2} \left(\frac{\eta \hat{\omega}}{\kappa} \right) - Y_{\hat{k}+2} \left(\frac{\eta \hat{\omega}}{\kappa} \right) \right] & -\eta^2 \hat{\omega}^2 \left[J_{\hat{k}-2}(\eta \hat{\omega}) + J_{\hat{k}+2}(\eta \hat{\omega}) \right] & -\eta^2 \hat{\omega}^2 \left[Y_{\hat{k}-2}(\eta \hat{\omega}) + Y_{\hat{k}+2}(\eta \hat{\omega}) \right] \end{bmatrix}$$

References

- [1] J. Li, Y. Lu, Y.F. Lee, Debonding detection in CFRP-reinforced steel structures using anti-symmetrical guided waves, Compos. Struct. 253 (2020).
- [2] Z. Su, L. Ye, Y. Lu, Guided Lamb waves for identification of damage in composite structures: a review, J. Sound Vib. 295 (2006) 753–780.
- [3] S. Shoja, Guided wave-based approach for health monitoring of composite structures: Application to wind turbine blades, 2018.
- [4] C.Q. Gómez Muñoz, F.P. García Marquez, B. Hernandez Crespo, K. Makaya, Structural health monitoring for delamination detection and location in wind turbine blades employing guided waves, Wind Energy 22 (2019) 698–711.
- [5] S. Cantero-Chinchilla, G. Aranguren, J.M. Royo, M. Chiachio, J. Etxaniz, A. Calvo-Echenique, Structural health monitoring using ultrasonic guided-waves and the degree of health index, Sensors (Basel) 21 (2021).
- [6] F. Wang, S.C.M. Ho, G. Song, Modeling and analysis of an impact-acoustic method for bolt looseness identification, Mech. Syst. Sig. Process. 133 (2019).
- [7] G. Sha, H. Xu, M. Radzinski, M. Cao, W. Ostachowicz, Z. Su, Guided wavefield curvature imaging of invisible damage in composite structures, Mech. Syst. Sig. Process. 150 (2021).
- [8] M. Palacz, A. Zak, M. Krawczuk, FEM-based wave propagation modelling for SHM: certain numerical issues in 1d structures, Materials (Basel) 13 (2020).
- [9] B. Lei, N. Wang, P. Xu, G. Song, New crack detection method for bridge inspection using UAV incorporating image processing, J. Aerosp. Eng. 31 (2018).
- [10] T. Kundu, S. Hu, W. Chen, L. Liu, X. Gao, Research of diagnosis sensors fault based on correlation analysis of the bridge structural health monitoring system, Health Monitor. Struct. Biol. Syst. (2010).
- [11] V.Y. Senyurek, Detection of cuts and impact damage at the aircraft wing slat by using Lamb wave method, Measurement 67 (2015) 10–23.
- [12] C.S. Sakaris, M. Bashir, Y. Yang, C. Michailides, J. Wang, J.S. Sakellarou, Diagnosis of damaged tendons on a 10 MW multibody floating offshore wind turbine platform via a response-only functional model based method, Eng. Struct. 242 (2021).
- [13] C.R. Farrar, K. Worden, An introduction to structural health monitoring, Philos. Trans. A Math Phys. Eng. Sci. 365 (2007) 303–315.
- [14] O. Avci, O. Abdeljaber, S. Kiranyaz, M. Hussein, M. Gabbouj, D.J. Inman, A review of vibration-based damage detection in civil structures: From traditional methods to Machine Learning and Deep Learning applications, Mech. Syst. Sig. Process. 147 (2021).
- [15] Z. Pang, M. Yuan, M.B. Wakin, A random demodulation architecture for sub-sampling acoustic emission signals in structural health monitoring, J. Sound Vib. 431 (2018) 390–404.
- [16] P. Mirgal, J. Pal, S. Banerjee, Online acoustic emission source localization in concrete structures using iterative and evolutionary algorithms, Ultrasonics 108 (2020), 106211.
- [17] J. dos Reis, C. Oliveira Costa, J. Sá da Costa, Strain gauges debonding fault detection for structural health monitoring, Struct. Control Health Monitor. 25 (2018).

- [18] Y. Wang, X. Zhu, H. Hao, J. Ou, Guided wave propagation and spectral element method for debonding damage assessment in RC structures, *J. Sound Vib.* 324 (2009) 751–772.
- [19] Y. Shao, L. Zeng, J. Lin, Damage detection of thick plates using trailing pulses at large frequency-thickness products, *Appl. Acoust.* 174 (2021).
- [20] P.W. Loveday, C.S. Long, D.A. Ramatlo, Ultrasonic guided wave monitoring of an operational rail track, *Struct. Health Monitor.* 19 (2019) 1666–1684.
- [21] M.M. Bahador, A. Zaimbashi, R. Rahgozar, Three-stage Lamb-wave-based damage localization algorithm in plate-like structures for structural health monitoring applications, *Signal Process.* 168 (2020).
- [22] Y. Shao, L. Zeng, J. Lin, W. Wu, H. Zhang, Trailing pulses self-focusing for ultrasonic-based damage detection in thick plates, *Mech. Syst. Sig. Process.* 119 (2019) 420–431.
- [23] H. Huo, J. He, X. Guan, A Bayesian fusion method for composite damage identification using Lamb wave, *Struct. Health Monitor.* (2020).
- [24] C. Yeung, C.T. Ng, Time-domain spectral finite element method for analysis of torsional guided waves scattering and mode conversion by cracks in pipes, *Mech. Syst. Sig. Process.* 128 (2019) 305–317.
- [25] M. Ho, S. El-Borgi, D. Patil, G. Song, Inspection and monitoring systems subsea pipelines: a review paper, *Struct. Health Monitor.* 19 (2019) 606–645.
- [26] H. Zhang, J. Zhang, G. Fan, H. Zhang, W. Zhu, Q. Zhu, R. Zheng, The auto-correlation of ultrasonic lamb wave phased array data for damage detection, *Metals* 9 (2019).
- [27] J.L. Rose, Ultrasonic guided waves in solid media, Cambridge University Press, UK, 2014.
- [28] W. Zhou, H. Li, F.-G. Yuan, Guided wave generation, sensing and damage detection using in-plane shear piezoelectric wafers, *Smart Mater. Struct.* 23 (2014).
- [29] Y. Yang, C.-T. Ng, A. Kotousov, H. Sohn, H.J. Lim, Second harmonic generation at fatigue cracks by low-frequency Lamb waves: experimental and numerical studies, *Mech. Syst. Sig. Process.* 99 (2018) 760–773.
- [30] C. Zhou, Z. Su, L. Cheng, Quantitative evaluation of orientation-specific damage using elastic waves and probability-based diagnostic imaging, *Mech. Syst. Sig. Process.* 25 (2011) 2135–2156.
- [31] J. Park, Y. Cho, A study on guided wave tomographic imaging for defects on a curved structure, *J. Visualization* 22 (2019) 1081–1092.
- [32] Q. Huan, M. Chen, F. Li, A high-sensitivity and long-distance structural health monitoring system based on bidirectional SH wave phased array, *Ultrasonics* 108 (2020), 106190.
- [33] S.J. Lw, Fundamentals of ultrasonic phased arrays, *Mod. Phys. Lett. B* 22 (11) (2008) 917–921.
- [34] B. Yoo, A.S. Purekar, Y. Zhang, D.J. Pines, Piezoelectric-paint-based two-dimensional phased sensor arrays for structural health monitoring of thin panels, *Smart Mater. Struct.* 19 (2010).
- [35] Z. Liu, K. Sun, G. Song, C. He, B. Wu, Damage localization in aluminum plate with compact rectangular phased piezoelectric transducer array, *Mech. Syst. Sig. Process.* 70–71 (2016) 625–636.
- [36] R.K. Munian, D. Roy Mahapatra, S. Gopalakrishnan, Ultrasonic guided wave scattering due to delamination in curved composite structures, *Composite Structures*, 239 (2020).
- [37] H.C. Li Longtao, Wu Bin, Detection of a longitudinal defect in a pipe based on guided circumferential waves techniques, *ACTA ACUSTICA (Chinese version)*, (2005) 343–348.
- [38] M.L.B. Pavlakovic, DISPERSE User's Manual, Non-Destructive Testing Laboratory, Department of Mechanical Engineering, Imperial College London, UK, 2013.
- [39] H. Taheri, A.A. Hassen, Nondestructive ultrasonic inspection of composite materials: a comparative advantage of phased array ultrasonic, *Appl. Sci.* 9 (2019).
- [40] W. Wang, H. Zhang, J.P. Lynch, C.E.S. Cesnik, H. Li, Experimental and numerical validation of guided wave phased arrays integrated within standard data acquisition systems for structural health monitoring, *Struct. Control Health Monitor.* 25 (2018).
- [41] S. Zhang, W. Fan, An efficient semi-analytical formulation for the Lamb-like waves in layered waveguides based on global discretization, *Comput. Struct.* 249 (2021).
- [42] Q. Wang, X. Yan, S. Ding, Y. Huo, Research on the interfacial behaviors of plate-type dispersion nuclear fuel elements, *J. Nucl. Mater.* 399 (2010) 41–54.
- [43] B.R. Mace, E. Manconi, Modeling wave propagation in two-dimensional structures using finite element analysis, *J. Sound Vib.* 318 (2008) 884–902.
- [44] F. Moser, L.J. Jacobs, J. Qu, Modeling elastic wave propagation in waveguides with the finite element method, *NDT & E Int.* 32 (1999) 225–234.
- [45] C. Hu, B. Yang, F.Z. Xuan, J. Yan, Y. Xiang, Damage orientation and depth effect on the guided wave propagation behavior in 30CrMo steel curved plates, *Sensors (Basel)* 20 (2020).
- [46] V.G.L. Yu, In-situ optimized PWAS phased arrays for Lamb wave structural health monitoring, *J. Mech. Mater. Struct.* 2 (2007) 459.